Acta Mech 229, 5093–5120 (2018)
https://doi.org/10.1007/s00707-018-2284-2

ORIGINAL PAPER

M. N. Rao · R. Schmidt · K. U. Schröder

Static and dynamic FE analysis of piezolaminated composite shells considering electric field nonlinearity under thermo-electro-mechanical loads

Received: 29 August 2017 / Revised: 19 July 2018 / Published online: 25 October 2018

Abstract The present article focuses on the static and dynamic finite element simulations of smart piezolaminated composite shell structures considering strong electric field nonlinearity under thermo-electro-mechanical loads. To model the electromechanical behaviour of piezoelectric patches or layers under large applied electric fields more efficiently, two-way coupled rotationally invariant second-order nonlinear constitutive relations are used in the variational principle approach. Furthermore, the nonlinear piezoelectric element formulations are further extended to capture the response under temperature gradients. Quadratic and cubic polynomial approximations are deemed to represent the electric potential and temperature fields, respectively. Validation of the present element formulation has been done in comparison to experimental and numerical investigations of those available in the literature. Moreover, numerical simulations are performed to study the large electric field nonlinearities of piezolaminated structures in static and dynamic as well as active vibration control problems under both mechanical and thermal loads. The numerical simulations have shown that using the piezoelectric nonlinearity, both the static shape control and vibration suppression either under mechanical or thermal loads can be accomplished at much lower actuation voltages than estimated by the linear model.

1 State of art

Smart materials (e.g. piezoelectric, magneto-restrictive, shape memory alloys, etc.) have gained attentiveness for their use in sensors, actuators, noise, vibration, shape and position control, non-destructive testing and health monitoring systems. Among these, use of piezoelectric material for sensing and distributed actuation by possessing self-controlling capabilities for the development of high-performing lightweight flexible structures has attracted many researchers in recent years. In the aeronautical and space engineering fields, vibration suppression and flutter control by active piezoelectric materials has gained significant attention as the development of smart skins for helicopter rotor blades and aeroelastic wings, and also other intelligent, flexible structures (see [2,5,8,13,29,30,36,39]). On the other hand, lightweight thin-walled laminated smart composite structures have found wide applications. Therefore, laminated shell-type structures bonded with piezoelectric layers have been focused. Furthermore, a challenge exists in the accurate prediction of the static and dynamic behaviours of smart piezolaminated structures in order to design the smart systems effectively. There is a substantial body of literature (see review articles of [9,16]) on the modelling and analysis of piezolaminated composite structures, much of which exploits linear behaviour either in geometrically (i.e. valid for small deformations) or materially (i.e. considering linear piezoelectricity). Most of the literature is based on linear constitutive relations to describe the piezomechanical coupling. This linear constitutive relation approach is appropriate for weak electromechanical coupling and low electric fields. Some piezoceramics and lithium niobate etc. show

M. N. Rao (✉) · R. Schmidt · K. U. Schröder
Institute of Structural Mechanics and Lightweight Design, RWTH Aachen University, Aachen, Germany
E-mail: rao.mekala@sla.rwth-aachen.de

constitutive nonlinearity under strong electric fields by virtue of ferroelectric hysteresis and repolarisation, which was justified experimentally by [24,26].

Numerous researchers have studied analytical modelling of the experimentally observed nonlinear behaviour of piezoelectrics. However, static and transient analysis of laminated composites integrated with piezoelectric layers or patches considering strong electric field nonlinearities is carried out by only very few authors. To model the strong electric field reversible nonlinearities in piezoelectrics [15,26,41] proposed higher-order polynomial equations in constitutive modelling. Ge and Jouaneh [7] and Roysten and Houston [33] studied irreversible nonlinearities and rate-independent hysteresis and further derived analytical equations for nonlinear piezoelectricity. A regular basis by taking cubic terms in the thermodynamic Gibbs potential was introduced by [15] to acquire the nonlinear constitutive relations of piezomechanical coupling. Tiersten [41] expressed electromechanical coupling for the case of small deformations and strong electric fields by rotationally invariant nonlinear constitutive relations. Independent polynomial expressions of second-order were derived by [46,47] to model the piezoelastic coupling in the *mm6* and *mm2* symmetry classes of piezoelectrics.

Strong electric field nonlinear piezoelectric behaviour in unimorph, bimorph and rainbow actuators was noticed in experiments by [45]. The analysis of piezoelectric actuators under large applied electric fields in both statics and dynamics by adopting classical beam theory can be found in the articles of [48,49]. They compared the experimental observations conducted by [45]. Achuthan et al. [1] developed a plane stress piezoelectric finite element (FE) model, wherein the dependence of piezoelectric constants on applied electric fields is considered to perform static shape control of composite beams. Yao et al. [50] considers the nonlinear electromechanical coupling equations of [15] in the framework of classical laminate theory (CLT) to develop mathematical expressions for the static response of simply supported piezolaminated plates under large applied electric fields. To account for shear deformations in laminates, Hong and Chopra [12] adopted first-order shear deformation (FOSD) theory. A similar study [50] was carried out for laminated composite plates bonded with piezopatches assuming piezoelectric coefficients to be a quadratic function of the applied electric field. Wagner et al. [43] and Samal et al. [34] conducted experiments on cantilevered piezoelectric beams to study nonlinear effects and concluded that despite the fact of applied weak electric fields, nonlinearity in piezoelectric materials is observed if the system is excited near resonance. This was further studied recently by developing an FE model using nonlinear elastic and piezoelectric constants by [27,28]. Thornburgh and Chattopadhyay [40] investigated static behaviour of piezolaminated plates by incorporating third-order shear deformation (TOSD) theory to address the shear deformations of laminates more precisely and further assumed linear dependence of piezoelectric coefficients on electric/strain fields to model the strong electric field nonlinearity. Almost identical modelling characteristics of [12] endorsed and developed a four-node plate element by [38] to investigate the static shape control of plates with piezopatches.

All the aforementioned models are based on equivalent single layers (ESL) theories to analyse the smart laminated composite plates integrated with nonlinear piezoelectric actuators. Layer-wise finite elements in the framework of 2-D multilayered piezolaminated plate theories provide accurate solutions; however, the associated cost in computations multiplies as the number of layers increases. Finite elements based on these layer-wise theories for laminated composites considering piezoelectric nonlinearities have been developed by [35]. Different from the present paper, they adopted the nonlinearity in the polarisation–electric field interaction and also assumed cubic polynomials for displacements and electric potentials. Very recently, Kapuria and Yaqoob Yasin [17] presented a finite element model by incorporating layer-wise zigzag and TOSD theories to study the static deformations of bimorph and sandwich piezolaminated plates accounting for the nonlinear electromechanical coupling relations of [41]; later active vibration control of laminated plates was investigated by [18].

Despite the fact that some studies have been reported in the literature, the study on laminated composite plates integrated with piezoelectric patches or layers considering strong electric field nonlinearity is still rarely addressed. Some analytical and numerical models are not accurate under strong electric fields [1,12,47–49] since they treat only one-way piezoelastic behaviour in nonlinear constitutive relations. In particular, the above-mentioned literature is limited to either 1-D beam or 2-D plate finite elements. The other type of nonlinearities are the aftereffects of the ferroelectric switching; usually, these are irreversible nonlinearities. Many piezoelectric materials are made from ferroelectric ceramic. For this class of materials, domain switching effects occur for large electric fields, see e.g. [19] and the references therein. These are not considered in the present work. Thus, it is restricted to moderate electric fields. A lot of research exists in the literature concerning the modelling of irreversible nonlinearities such as rate-independent hysteresis. However, the model proposed in the present article is based on the assumption of reversible nonlinearities, and this type of model is suitable when only quasi-static loading is considered, and it should be noted that in our model in

case of unloading minor hysteresis effects are neglected. However, in the majority of the static shape control and active vibration control problems, it is inevitable to apply strong electric fields to attain higher actuation authority. Therefore it is essential to adopt advanced finite element formulations for a precise prediction of response of piezolaminated structures considering strong electric field nonlinearities. In fact, no study has been carried out with thermal loads considering the electromechanical coupling under strong electric fields to analyse piezoelectric laminated structures. In the present paper, a 2D-shell finite element model is proposed to carry out static analysis of piezolaminated composite shells by incorporating nonlinear constitutive relations in order to describe the electromechanical coupling under strong electric fields. The nonlinearity in piezoelastic coupling is based on the assumptions of small strains and large electric fields in the rotationally invariant constitutive equations of [41]. The shell finite element based on the work of [20,44] and applied by [23,31] is extended to develop the numerical models for composite shells integrated with nonlinear piezoelectric actuators. A quadratic variation of the electric potential through the thickness is assumed to include electromechanical stiffness more accurately. A cubic polynomial over the thickness is deemed to represent temperature fields. Here, the element formulation is restricted to geometrically linear problems, in order to study and demonstrate exclusively the constitutive nonlinearity in piezomechanical coupling. The Newton–Raphson iteration and Newmark time integration techniques are used to solve the static and dynamic problems, respectively. Some numerical examples are presented to study the static shape and active vibration control problems using the developed nonlinear piezolaminated composite shell element under strong electric fields.

2 Basic equations and kinematics

2.1 Strain–displacement relations

In this shell element, small strains and small rotations of [6,11] are adopted in the framework of Reissner-Mindlin first-order transverse shear deformation (FOSD) hypothesis and the FE implementation of [44].

The four-node shell element with the global $\boldsymbol{g}_i$, the local $\boldsymbol{a}_\alpha$, the natural ξ–η and the orthonormal material $\boldsymbol{t}_i$ coordinate systems are shown in Fig. 1.

The Jacobian matrix $\boldsymbol{J}$ defines the relation between the orthonormal material coordinate system and the natural coordinate system and $\boldsymbol{r}_I$ is the position vector to the reference mid-surface in the initial configuration of node I. The position vector $\boldsymbol{R}$ to an arbitrary point on the director at the position (ξ, η) can be determined as

$$\boldsymbol{R}(\xi, \eta, z) = \boldsymbol{r}(\xi, \eta) + z\, \boldsymbol{d}(\xi, \eta), \tag{1}$$

where z denotes the thickness coordinate ranging from the bottom to the top of the considered shell and where $\boldsymbol{d}$ indicates the director. In the context of small strains and small rotations, the infinitesimal strain–tensor components based on the FOSD theory are expressed as (see [6,11])

$$\begin{aligned} \varepsilon_{\alpha\beta} &= \overset{0}{\varepsilon}_{\alpha\beta} + z\overset{1}{\varepsilon}_{\alpha\beta} + z^2\overset{2}{\varepsilon}_{\alpha\beta}, \\ \varepsilon_{\alpha 3} &= \overset{0}{\varepsilon}_{\alpha 3} + z\overset{1}{\varepsilon}_{\alpha 3}, \\ \varepsilon_{33} &= \overset{0}{\varepsilon}_{33}, \end{aligned} \tag{2}$$

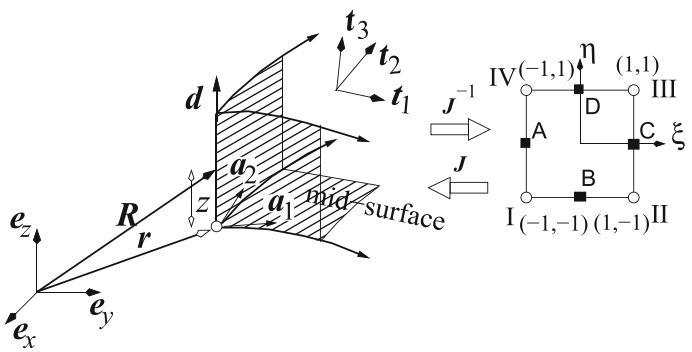

Fig. 1 Definition of the coordinate systems in the FRT element

where

$$
\begin{aligned}
2\overset{0}{\varepsilon}_{\alpha\beta} &= \boldsymbol{r}_{,\alpha}\cdot(\bar{\mathrm{r}}_{,\beta}-\boldsymbol{r}_{,\beta})+\boldsymbol{r}_{,\beta}\cdot(\bar{\mathrm{r}}_{,\alpha}-\boldsymbol{r}_{,\alpha}),\\
2\overset{1}{\varepsilon}_{\alpha\beta} &= \boldsymbol{r}_{,\alpha}\cdot(\bar{\mathrm{d}}_{,\beta}-\boldsymbol{d}_{,\beta})+\boldsymbol{r}_{,\beta}\cdot(\bar{\mathrm{d}}_{,\alpha}-\boldsymbol{d}_{,\alpha})+\boldsymbol{d}_{,\alpha}\cdot(\bar{\mathrm{r}}_{,\beta}-\boldsymbol{r}_{,\beta})+\boldsymbol{d}_{,\beta}\cdot(\bar{\mathrm{r}}_{,\alpha}-\boldsymbol{r}_{,\alpha}),\\
2\overset{0}{\varepsilon}_{\alpha 3} &= \boldsymbol{r}_{,\alpha}\cdot\bar{\mathrm{d}}+\boldsymbol{d}_{,\beta}\cdot\bar{\mathrm{r}}_{,\alpha}.
\end{aligned}
\tag{3}
$$

In Eq. (3), an overbar indicates vectors in the deformed configuration. Here, on behalf of thin-walled structures, the components $\overset{2}{\varepsilon}_{\alpha\beta}$ are neglected. With the presumption of an inextensible director $\overset{0}{\varepsilon}_{33}= 0$, and as a consequence of FOSD theory the components of $\overset{1}{\varepsilon}_{\alpha 3}$ become equal to zero as well.

2.2 Constitutive relations

The general rotationally invariant nonlinear equations of piezoelectricity in a 3D-system as prescribed by Tiersten [41] are given as

$$
\begin{Bmatrix}\varepsilon_{11}\\ \varepsilon_{22}\\ \varepsilon_{33}\\ 2\varepsilon_{12}\\ 2\varepsilon_{13}\\ 2\varepsilon_{23}\end{Bmatrix}=\begin{bmatrix}s_{11}&s_{12}&s_{13}&0&0&0\\ s_{12}&s_{22}&s_{23}&0&0&0\\ s_{13}&s_{23}&s_{33}&0&0&0\\ 0&0&0&s_{44}&0&0\\ 0&0&0&0&s_{55}&0\\ 0&0&0&0&0&s_{66}\end{bmatrix}\begin{Bmatrix}S_{11}\\ S_{22}\\ S_{33}\\ S_{12}\\ S_{13}\\ S_{23}\end{Bmatrix}+\begin{bmatrix}0&0&d_{31}\\ 0&0&d_{32}\\ 0&0&d_{33}\\ 0&0&0\\ d_{15}&0&0\\ 0&d_{15}&0\end{bmatrix}\begin{Bmatrix}E_1\\ E_2\\ E_3\end{Bmatrix}
$$
$$
+\begin{Bmatrix}\alpha_{11}\\ \alpha_{22}\\ \alpha_{33}\\ 0\\ 0\\ 0\end{Bmatrix}\Delta\boldsymbol{T}+\frac{1}{2}\begin{Bmatrix}b_{11}\\ b_{22}\\ b_{33}\\ 0\\ 0\\ 0\end{Bmatrix}|E_3|E_3,
\tag{4}
$$

$$
\begin{Bmatrix}D_1\\ D_2\\ D_3\end{Bmatrix}=\begin{bmatrix}0&0&0&0&d_{15}&0\\ 0&0&0&0&0&d_{15}\\ d_{31}&d_{32}&d_{33}&0&0&0\end{bmatrix}\begin{Bmatrix}S_{11}\\ S_{22}\\ S_{33}\\ S_{12}\\ S_{13}\\ S_{23}\end{Bmatrix}+\begin{bmatrix}\epsilon_{11}&0&0\\ 0&\epsilon_{22}&0\\ 0&0&\epsilon_{33}\end{bmatrix}\begin{Bmatrix}E_1\\ E_2\\ E_3\end{Bmatrix}
$$
$$
+\begin{bmatrix}\gamma_{11}&0&0\\ 0&\gamma_{22}&0\\ 0&0&\gamma_{33}\end{bmatrix}\Delta\boldsymbol{T}+\frac{1}{2}\begin{Bmatrix}0\\ 0\\ \varsigma_{33}\end{Bmatrix}|E_3|E_3,
\tag{5}
$$

where S_{ij} denotes the stress components, ε_{ij} the strain components, E_i and D_i are the electric field and displacement components, α_{ij} the thermal expansion strain constants, and γ_{ij} the thermoelectric constants, and $\Delta\boldsymbol{T}$ is the temperature difference. The constants s_{ij}, d_{ij} and ϵ_{ij} represent, respectively, the elastic compliance coefficients, piezoelectric strain coefficients , and dielectric constants, b_{ij} and ς_{ij} are the electroelastic strain and electroelastic susceptibility constants related to the quadratic electric fields in Eqs. (4) and (5). These constitutive Eqs. (4) and (5) have been derived by Tiersten [41] based on a cubic approximation of the Gibb's potential for coupled electro-thermo-mechanical 3-D continuum mechanics. This leads to second-order nonlinear equations involving quadratic term of the electric field E. Here, in view of the application to 2-D plate and shell problems, in the nonlinear term we have only considered the transverse electric field E_3.

For the present 2D-theory, the constitutive relations (4) and (5) are represented in the following standard manner

$$
\boldsymbol{S}=\boldsymbol{c\varepsilon}-\boldsymbol{e}^{\mathrm{T}}\boldsymbol{E}-\boldsymbol{\lambda}\Delta\boldsymbol{T}-\frac{1}{2}\hat{\boldsymbol{\beta}}|E_3|E_3,
\tag{6}
$$

$$
\boldsymbol{D}=\boldsymbol{e\varepsilon}+\boldsymbol{\epsilon}\boldsymbol{E}+\hat{\boldsymbol{\gamma}}\Delta\boldsymbol{T}+\frac{1}{2}\hat{\boldsymbol{\chi}}|E_3|E_3,
\tag{7}
$$

where $\boldsymbol{S}$ denotes the stress vector, $\boldsymbol{\varepsilon}$ the strain vector, $\boldsymbol{D}$ the electric displacement vector, $\boldsymbol{E}$ the electric field vector, $\Delta\boldsymbol{T}$ is the temperature difference:

$$\boldsymbol{S} = \begin{Bmatrix} S_{11} \\ S_{22} \\ S_{12} \\ S_{13} \\ S_{23} \end{Bmatrix}, \qquad \boldsymbol{\varepsilon} = \begin{Bmatrix} \varepsilon_{11} \\ \varepsilon_{22} \\ 2\varepsilon_{12} \\ 2\varepsilon_{13} \\ 2\varepsilon_{23} \end{Bmatrix},$$
$$\boldsymbol{D} = \begin{Bmatrix} D_1 \\ D_2 \\ D_3 \end{Bmatrix}, \quad \text{and} \quad \boldsymbol{E} = \begin{Bmatrix} E_1 \\ E_2 \\ E_3 \end{Bmatrix}. \tag{8}$$

Concerning the various matrices in Eqs. (6) and (7) $\boldsymbol{c}$ denotes the elasticity matrix for anisotropic material, $\boldsymbol{d}$ is the piezoelectric constant matrix, $\boldsymbol{\epsilon}$ is the dielectric constant matrix, $\boldsymbol{\lambda}$ is the thermal stress coefficient vector, $\hat{\boldsymbol{\gamma}}$ is the pyroelectric coefficient vector:

$$\boldsymbol{c} = \left[\begin{array}{ccc|cc} c_{11} & c_{12} & 0 & 0 & 0 \\ c_{12} & c_{22} & 0 & 0 & 0 \\ 0 & 0 & c_{33} & 0 & 0 \\ \hline 0 & 0 & 0 & c_{44} & 0 \\ 0 & 0 & 0 & 0 & c_{55} \end{array}\right] = \begin{bmatrix} [C_1] & \mathbf{0}_{(3\times2)} \\ \mathbf{0}_{(2\times3)} & [C_2] \end{bmatrix}, \tag{9}$$

$$\boldsymbol{e}^{\mathrm{T}} = \left[\begin{array}{cc|c} 0 & 0 & e_{13} \\ 0 & 0 & e_{13} \\ 0 & 0 & 0 \\ \hline e_{41} & 0 & 0 \\ 0 & e_{41} & 0 \end{array}\right] = \begin{bmatrix} \mathbf{0}_{(3\times2)} & [\boldsymbol{e}_1] \\ [\boldsymbol{e}_2] & \mathbf{0}_{(2\times1)} \end{bmatrix}, \tag{10}$$

$$\boldsymbol{\epsilon} = \left[\begin{array}{cc|c} \hat{\epsilon}_1 & 0 & 0 \\ 0 & \hat{\epsilon}_2 & 0 \\ \hline 0 & 0 & \hat{\epsilon}_3 \end{array}\right] = \begin{bmatrix} [\boldsymbol{\epsilon}_1] & \mathbf{0}_{(2\times1)} \\ \mathbf{0}_{(1\times2)} & [\boldsymbol{\epsilon}_2] \end{bmatrix}, \tag{11}$$

$$\boldsymbol{\lambda} = \left\{\begin{array}{c} \lambda_{11} \\ \lambda_{22} \\ 0 \\ \hline 0 \\ 0 \end{array}\right\} = \begin{Bmatrix} [\boldsymbol{\lambda_1}] \\ 0 \end{Bmatrix}, \tag{12}$$

$$\hat{\boldsymbol{\gamma}} = \left\{\begin{array}{c} 0 \\ 0 \\ \hline \hat{\gamma}_3 \end{array}\right\} = \begin{Bmatrix} 0 \\ [\boldsymbol{\gamma_1}] \end{Bmatrix}. \tag{13}$$

The electroelastic strain and susceptibility constant vectors related to the quadratic electric fields are:

$$\hat{\boldsymbol{\beta}} = \left\{\begin{array}{c} \beta_{31} \\ \beta_{32} \\ 0 \\ \hline 0 \\ 0 \end{array}\right\} = \begin{Bmatrix} [\boldsymbol{\beta_1}] \\ 0 \end{Bmatrix}, \tag{14}$$

$$\hat{\boldsymbol{\chi}} = \left\{\begin{array}{c} 0 \\ 0 \\ \hline \chi_3 \end{array}\right\} = \begin{Bmatrix} 0 \\ [\boldsymbol{\chi_1}] \end{Bmatrix}. \tag{15}$$

The elasticity constants used in the above Eq. (9) are defined in terms of material parameters as

$$c_{11} = \frac{E_1}{1 - \nu_{12}\nu_{21}}, \quad c_{22} = \frac{E_2}{1 - \nu_{12}\nu_{21}}, \tag{16}$$

$$c_{12} = \frac{\nu_{12} E_2}{1 - \nu_{12}\nu_{21}}, \quad c_{33} = G_{12}, \tag{17}$$

$$c_{44} = \kappa G_{12}, \quad c_{55} = \kappa \frac{E_2}{2(1 + \nu_{23})}, \tag{18}$$

where $\kappa = \frac{5}{6}$ is introduced as a shear correction factor to account for the over-predicted transverse shear deformation energy of the first-order shear deformation theory and $\nu_{21} = \nu_{12}\frac{E_2}{E_1}$. The other variables in Eqs. (6) and (7) are

$$\beta_{31} = c_{11}b_{31} + c_{12}b_{32}, \quad \beta_{32} = c_{12}b_{31} + c_{22}b_{32}, \tag{19}$$

$$e_{31} = c_{11}d_{31} + c_{12}d_{32}, \quad e_{32} = c_{12}d_{31} + c_{22}d_{32}, \tag{20}$$

$$\lambda_{11} = c_{11}\alpha_{11} + c_{12}\alpha_{22}, \quad \lambda_{22} = c_{12}\alpha_{11} + c_{22}\alpha_{22}, \quad \hat{\gamma}_3 = \gamma_{33} - d_{31}\alpha_{11} - d_{32}\alpha_{22}, \tag{21}$$

$$e_{14} = c_{55}d_{15}, \quad e_{15} = c_{66}d_{15}, \quad \hat{\epsilon}_1 = \epsilon_{11} - d_{15}e_{15}, \quad \hat{\epsilon}_2 = \epsilon_{22} - d_{24}e_{24}, \tag{22}$$

$$\hat{\epsilon}_3 = \epsilon_{33} - d_{31}\beta_{31} - d_{32}\beta_{32}, \quad \chi_3 = \varsigma_{33} - d_{31}e_{31} - d_{32}e_{32}, \tag{23}$$

The stress, strain and elasticity matrices in the material coordinate system are obtained, if the material principal axes are not coincident with the material coordinate system, as

$$\boldsymbol{\varepsilon} = \boldsymbol{T}^{-1}\boldsymbol{\varepsilon_m}, \quad \boldsymbol{S} = \boldsymbol{T}^T\boldsymbol{S_m}, \quad \boldsymbol{c} = \boldsymbol{T}^T\boldsymbol{c_m}\boldsymbol{T}, \tag{24}$$

where the subscript $\boldsymbol{m}$ represents the material principle axes and the transformation matrix $\boldsymbol{T}$ is given by

$$\boldsymbol{T} = \begin{bmatrix} \cos^2\theta & \sin^2\theta & \sin\theta\cos\theta & 0 & 0 \\ \sin^2\theta & \cos^2\theta & -\sin\theta\cos\theta & 0 & 0 \\ -\sin 2\theta & \sin 2\theta & \cos 2\theta & 0 & 0 \\ 0 & 0 & 0 & \cos\theta & \sin\theta \\ 0 & 0 & 0 & -\sin\theta & \cos\theta \end{bmatrix}. \tag{25}$$

Using the following relation thermal fields can be expressed by temperature differences

$$\boldsymbol{h} = \boldsymbol{\kappa}\nabla\vartheta, \tag{26}$$

where $\boldsymbol{\kappa}$ is the heat conductivity matrix:

$$\boldsymbol{\kappa} = \left[\begin{array}{cc|c} \kappa_1 & 0 & 0 \\ 0 & \kappa_1 & 0 \\ \hline 0 & 0 & \kappa_3 \end{array}\right] = \begin{bmatrix} [\boldsymbol{\kappa}_1] & \mathbf{0}_{(2\times 1)} \\ \mathbf{0}_{(1\times 2)} & [\boldsymbol{\kappa}_2] \end{bmatrix}. \tag{27}$$

In a similar manner, the heat conductivity and thermal stress coefficient vectors require a transformation from principal material axes to the material coordinate system as

$$\boldsymbol{\lambda} = [\boldsymbol{T}]^{\mathrm{T}}\boldsymbol{\lambda}_m, \quad \boldsymbol{\kappa} = [\boldsymbol{T}_{\boldsymbol{\kappa}}]^{\mathrm{T}}\boldsymbol{\kappa}_m[\boldsymbol{T}_{\boldsymbol{\kappa}}]. \tag{28}$$

Here the transformation matrix $[\boldsymbol{T}_3]$ is given by

$$[\boldsymbol{T}_{\boldsymbol{\kappa}}] = \begin{bmatrix} \cos\theta & \sin\theta & 0 \\ -\sin\theta & \cos\theta & 0 \\ 0 & 0 & 1 \end{bmatrix}. \tag{29}$$

2.3 Electric field equations

The electric field can be introduced as negative gradient of the scalar electric potential ϕ as

$$\{\boldsymbol{E}\} = -\{\nabla\phi\}. \tag{30}$$

As observed in the analytical three-dimensional solutions [21], a quadratic variation of the electric potential across the thickness is considered to model the bending-induced electromechanical stiffness very accurately:

$$\phi(x, y, z) = \overset{0}{\phi}(x, y) + z\overset{1}{\phi}(x, y) + z^2\overset{2}{\phi}(x, y), \tag{31}$$

By using Eqs. (30) and (32), one obtains the electric field as

$$\begin{aligned} \boldsymbol{E}_\alpha &= \overset{0}{\boldsymbol{E}}_\alpha + z\overset{1}{\boldsymbol{E}}_\alpha + z^2\overset{2}{\boldsymbol{E}}_\alpha, \\ \boldsymbol{E}_3 &= \overset{0}{\boldsymbol{E}}_3 + z\overset{1}{\boldsymbol{E}}_3 . \end{aligned} \tag{32}$$

2.4 Temperature difference distribution

In this finite element model, the temperature distribution in transverse direction is treated by adopting a cubic variation of the temperature differences $\Delta\boldsymbol{T} = \boldsymbol{\vartheta}$. Thus,

$$\vartheta(z) = \overset{0}{\vartheta} + z\overset{1}{\vartheta} + z^2\overset{2}{\vartheta} + z^3\overset{3}{\vartheta}. \tag{33}$$

As a consequence of Eq. (33), the temperature gradients $\boldsymbol{\varphi}$ are expressed as

$$\begin{aligned} \boldsymbol{\varphi}_\alpha &= \overset{0}{\boldsymbol{\varphi}}_\alpha + z\overset{1}{\boldsymbol{\varphi}}_\alpha + z^2\overset{2}{\boldsymbol{\varphi}}_\alpha + z^3\overset{3}{\boldsymbol{\varphi}}_\alpha, \\ \boldsymbol{\varphi}_3 &= \overset{0}{\boldsymbol{\varphi}}_3 + z\overset{1}{\boldsymbol{\varphi}}_3 + z^2\overset{2}{\boldsymbol{\varphi}}_3 . \end{aligned} \tag{34}$$

To overcome some discrepancies in physical interpretation of the assumed cubic polynomial distribution which contains four thermal degrees of freedom $\overset{0}{\vartheta}$, $\overset{1}{\vartheta}$, $\overset{2}{\vartheta}$ and $\overset{3}{\vartheta}$, these degrees of freedom are transformed to temperature on bottom and top surfaces, and the transverse gradients on the bottom and top surfaces, respectively, $\overset{-}{\vartheta}$, $\overset{+}{\vartheta}$, $\overset{-}{\varphi}_3$ and $\overset{+}{\varphi}_3$. With these degrees of freedom boundary conditions for the temperature on both surfaces can be enforced, and additionally the heat flux into and out of the shell can be controlled.

This can be formulated in matrix form as

$$\check{\boldsymbol{\vartheta}} = \boldsymbol{L}^{\vartheta}\,\boldsymbol{\vartheta}, \tag{35}$$

where

$$\boldsymbol{\vartheta} = \left\{ \overset{-}{\vartheta} \quad \overset{+}{\vartheta} \quad \overset{-}{\varphi}_3 \quad \overset{+}{\varphi}_3 \right\}^{\mathrm{T}}, \tag{36}$$

$$\check{\boldsymbol{\vartheta}} = \left\{ \overset{0}{\vartheta} \quad \overset{1}{\vartheta} \quad \overset{2}{\vartheta} \quad \overset{3}{\vartheta} \right\}^{\mathrm{T}}, \tag{37}$$

and $\boldsymbol{L}^{\vartheta}$ is the conversion matrix for the temperature field. The matrix $\boldsymbol{L}^{\vartheta}$ is given in Appendix A.

3 Finite element formulation

The variational formulation of the electromechanically coupled 3D boundary value problem can be written as

$$\int_V (\boldsymbol{S} : \delta\boldsymbol{\varepsilon} - \boldsymbol{D} \cdot \delta\boldsymbol{E})\, \mathrm{d}\boldsymbol{V} = \int_A (\boldsymbol{T} \cdot \delta\boldsymbol{v} + \boldsymbol{Q}\delta\phi)\, \mathrm{d}\boldsymbol{A} + \int_V (\boldsymbol{\rho}\,(\boldsymbol{b} - \ddot{\boldsymbol{v}})) \cdot \delta\boldsymbol{v}\mathrm{d}\boldsymbol{V}, \tag{38}$$

where $\boldsymbol{S}$ is the second Piola–Kirchhoff stress tensor, $\boldsymbol{D}$ is the dielectric displacement vector, $\delta\boldsymbol{\varepsilon}$ is the virtual Green–Lagrange strain tensor, $\delta\boldsymbol{E}$ is the virtual electric field vector, $\boldsymbol{T}$ is the traction vector on the boundary, Q is the surface related electric charge density, ρ is the mass density, b is the body force density, $\ddot{\boldsymbol{v}}$ is the acceleration vector, $\delta\boldsymbol{v}$ and $\delta\phi$ are the virtual displacement vector and electric potential, respectively. In this finite element shear locking is eliminated by assumed natural strain (ANS) method which was initially proposed by [14,25] (see [31] for further details). The enhanced assumed strain(EAS) method is used to enhance the shell element behaviour and to avoid the volume locking. This EAS method was first proposed by Simo and Rifai [37]. An enhanced quantity, which consists of the kinematically obtained value $\square$ and the enhancing part $\tilde{\square}$, is denoted by $\hat{\square}$. Thus,

$$\hat{\boldsymbol{\varepsilon}} = \boldsymbol{\varepsilon} + \tilde{\boldsymbol{\varepsilon}}. \tag{39}$$

The volume integral in Eq. (38) is reduced to a surface integral by performing the transverse integration analytically. The internal virtual work with both enhanced and kinematically obtained strains can be rewritten in the form

$$\begin{aligned}\int_V \left(\boldsymbol{S} : \delta\hat{\boldsymbol{\varepsilon}} - \boldsymbol{D} \cdot \delta\boldsymbol{E}\right) \mathrm{d}\boldsymbol{V} = &\int_\Omega \{\delta\boldsymbol{\mathcal{E}}_{\boldsymbol{\varepsilon}}\}^{\mathrm{T}}(\mathbb{C}_{\boldsymbol{c}}\{\boldsymbol{\mathcal{E}}_{\boldsymbol{\varepsilon}}\} + \mathbb{C}_{\boldsymbol{c}}\{\tilde{\boldsymbol{\mathcal{E}}}_{\boldsymbol{\varepsilon}}\} + \mathbb{C}_{\boldsymbol{e}}\{\boldsymbol{\mathcal{E}}_{\boldsymbol{E}}\} + \mathbb{C}_{\boldsymbol{\lambda}}\{\boldsymbol{\mathcal{E}}_{\boldsymbol{t}}\} + \mathbb{C}_{\boldsymbol{\beta}}\{\boldsymbol{\mathcal{E}}_{\boldsymbol{E}}\})\, \mathrm{d}\Omega \\ &+ \int_\Omega \{\delta\tilde{\boldsymbol{\mathcal{E}}}_{\boldsymbol{\varepsilon}}\}^{\mathrm{T}}(\mathbb{C}_{\boldsymbol{c}}\{\boldsymbol{\mathcal{E}}_{\boldsymbol{\varepsilon}}\} + \mathbb{C}_{\boldsymbol{c}}\{\tilde{\boldsymbol{\mathcal{E}}}_{\boldsymbol{\varepsilon}}\} + \mathbb{C}_{\boldsymbol{e}}\{\boldsymbol{\mathcal{E}}_{\boldsymbol{E}}\} + \mathbb{C}_{\boldsymbol{\lambda}}\{\boldsymbol{\mathcal{E}}_{\boldsymbol{t}}\} + \mathbb{C}_{\boldsymbol{\beta}}\{\boldsymbol{\mathcal{E}}_{\boldsymbol{E}}\})\, \mathrm{d}\Omega \\ &+ \int_\Omega \{\delta\boldsymbol{\mathcal{E}}_{\boldsymbol{E}}\}^{\mathrm{T}}(\mathbb{C}_{\boldsymbol{e}}\{\boldsymbol{\mathcal{E}}_{\boldsymbol{\varepsilon}}\} + \mathbb{C}_{\boldsymbol{e}}\{\tilde{\boldsymbol{\mathcal{E}}}_{\boldsymbol{\varepsilon}}\} + \mathbb{C}_{\boldsymbol{\epsilon}}\{\boldsymbol{\mathcal{E}}_{\boldsymbol{E}}\} + \mathbb{C}_{\boldsymbol{\gamma}}\{\boldsymbol{\mathcal{E}}_{\boldsymbol{t}}\} + \mathbb{C}_{\boldsymbol{\chi}}\{\boldsymbol{\mathcal{E}}_{\boldsymbol{E}}\})\, \mathrm{d}\Omega,\end{aligned} \tag{40}$$

where

$$\mathbb{C}_{\boldsymbol{c}} = \begin{bmatrix} \overset{0}{[C_1]} & \overset{1}{[C_1]} & \\ \overset{1}{[C_1]} & \overset{2}{[C_1]} & \mathbf{0}_{(6\times2)} \\ \mathbf{0}_{(2\times6)} & & \overset{0}{[C_2]} \end{bmatrix}, \tag{41}$$

$$\mathbb{C}_{\boldsymbol{e}} = -\begin{bmatrix} & & \overset{0}{[\boldsymbol{e}_1^P]} & \overset{1}{[\boldsymbol{e}_1^P]} \\ & \mathbf{0}_{(6\times6)} & \overset{1}{[\boldsymbol{e}_1^P]} & \overset{2}{[\boldsymbol{e}_1^P]} \\ \overset{0}{[\boldsymbol{e}_2^P]} & \overset{1}{[\boldsymbol{e}_2^P]} & \overset{2}{[\boldsymbol{e}_2^P]} & \mathbf{0}_{(2\times2)} \end{bmatrix}, \tag{42}$$

$$\mathbb{C}_{\boldsymbol{\lambda}} = -\begin{bmatrix} \overset{0}{[\boldsymbol{\lambda}_1]} & \overset{1}{[\boldsymbol{\lambda}_1]} & \overset{2}{[\boldsymbol{\lambda}_1]} & \overset{3}{[\boldsymbol{\lambda}_1]} \\ \overset{1}{[\boldsymbol{\lambda}_1]} & \overset{2}{[\boldsymbol{\lambda}_1]} & \overset{3}{[\boldsymbol{\lambda}_1]} & \overset{4}{[\boldsymbol{\lambda}_1]} \\ \multicolumn{4}{c}{\mathbf{0}_{(2\times4)}} \end{bmatrix}, \tag{43}$$

$$\mathbb{C}_{\boldsymbol{\beta}} = -\begin{bmatrix} & \overset{0}{[\boldsymbol{\beta}_1^P]} & \overset{1}{[\boldsymbol{\beta}_1^P]} \\ \mathbf{0}_{(6\times6)} & \overset{1}{[\boldsymbol{\beta}_1^P]} & \overset{2}{[\boldsymbol{\beta}_1^P]} \\ \mathbf{0}_{(2\times6)} & \mathbf{0}_{(2\times2)} & \end{bmatrix}, \tag{44}$$

$$\mathbb{C}_{\boldsymbol{\epsilon}} = -\begin{bmatrix} \overset{0}{[\boldsymbol{\epsilon}_1^P]} & \overset{1}{[\boldsymbol{\epsilon}_1^P]} & \overset{2}{[\boldsymbol{\epsilon}_1^P]} & \\ \overset{1}{[\boldsymbol{\epsilon}_1^P]} & \overset{2}{[\boldsymbol{\epsilon}_1^P]} & \overset{3}{[\boldsymbol{\epsilon}_1^P]} & \mathbf{0}_{(6\times2)} \\ \overset{2}{[\boldsymbol{\epsilon}_1^P]} & \overset{3}{[\boldsymbol{\epsilon}_1^P]} & \overset{4}{[\boldsymbol{\epsilon}_1^P]} & \\ & & & \overset{0}{[\boldsymbol{\epsilon}_1^P]} & \overset{1}{[\boldsymbol{\epsilon}_1^P]} \\ & \mathbf{0}_{(2\times6)} & & \overset{1}{[\boldsymbol{\epsilon}_1^P]} & \overset{2}{[\boldsymbol{\epsilon}_1^P]} \end{bmatrix}, \tag{45}$$

$$\mathbb{C}_{\chi} = -\begin{bmatrix} \mathbf{0}_{(6\times6)} & \mathbf{0}_{(6\times2)} \\ \mathbf{0}_{(2\times6)} & \begin{matrix} [{}^{0}_{1}\boldsymbol{\chi}^{P}] & [{}^{1}_{1}\boldsymbol{\chi}^{P}] \\ [{}^{1}_{1}\boldsymbol{\chi}^{P}] & [{}^{2}_{1}\boldsymbol{\chi}^{P}] \end{matrix} \end{bmatrix}, \tag{46}$$

$$\mathbb{C}_{\gamma} = -\begin{bmatrix} \mathbf{0}_{(6\times4)} \\ \begin{matrix} [{}^{0}_{1}\boldsymbol{\gamma}^{P}] & [{}^{1}_{1}\boldsymbol{\gamma}^{P}] & [{}^{2}_{1}\boldsymbol{\gamma}^{P}] & [{}^{3}_{1}\boldsymbol{\gamma}^{P}] \\ [{}^{1}_{1}\boldsymbol{\gamma}^{P}] & [{}^{2}_{1}\boldsymbol{\gamma}^{P}] & [{}^{3}_{1}\boldsymbol{\gamma}^{P}] & [{}^{4}_{1}\boldsymbol{\gamma}^{P}] \end{matrix} \end{bmatrix}, \tag{47}$$

and

$$\{\delta\boldsymbol{\mathcal{E}}_{\boldsymbol{\varepsilon}}\}^{\mathrm{T}} = \left\{\delta{}^{0}_{11}\varepsilon, \delta{}^{0}_{22}\varepsilon, 2\delta{}^{0}_{12}\varepsilon, \delta{}^{1}_{11}\varepsilon, \delta{}^{1}_{22}\varepsilon, 2\delta{}^{1}_{12}\varepsilon, 2\delta{}^{0}_{13}\varepsilon, 2\delta{}^{0}_{23}\varepsilon\right\}, \tag{48}$$

$$\{\delta\boldsymbol{\mathcal{E}}_{\boldsymbol{E}}\}^{\mathrm{T}} = \left\{\delta{}^{0}_{1}E^{P}, \delta{}^{0}_{2}E^{P}, \delta{}^{1}_{1}E^{P}, \delta{}^{1}_{2}E^{P}, \delta{}^{2}_{1}E^{P}, \delta{}^{2}_{2}E^{P}, \delta{}^{0}_{3}E^{P}, \delta{}^{1}_{3}E^{P}\right\}. \tag{49}$$

The variational formulation of the thermal field can be expressed as

$$\int_{V} \boldsymbol{h}\cdot\delta\boldsymbol{\varphi}\,\mathrm{d}\boldsymbol{V} = \int_{\partial V} \boldsymbol{n}\cdot\boldsymbol{h}\,\delta\vartheta\,\mathrm{d}\boldsymbol{A}, \tag{50}$$

where $\boldsymbol{\varphi}$ is the temperature gradient which is equal to the gradient of the temperature difference $\nabla\vartheta$. The heat flux resultant vector $\{\boldsymbol{h}\}$ can be expressed equivalently by reducing the volume integral of the first term of LHS of Eq. (50) to a surface integral, with implicitly including the transverse integration as

$$\int_{V} \boldsymbol{h}\cdot\delta\boldsymbol{\varphi}\,d\boldsymbol{V} = \int_{\Omega} \delta\boldsymbol{\mathcal{E}}_{\boldsymbol{t}}{}^{\mathrm{T}}\mathbb{C}_{\boldsymbol{\kappa}}\boldsymbol{\mathcal{E}}_{\boldsymbol{t}}\,\mathrm{d}\Omega, \tag{51}$$

with

$$\mathbb{C}_{\boldsymbol{\kappa}} = -\begin{bmatrix} \begin{matrix} [{}^{0}_{1}\boldsymbol{\kappa}] & [{}^{1}_{1}\boldsymbol{\kappa}] & [{}^{2}_{1}\boldsymbol{\kappa}] & [{}^{3}_{1}\boldsymbol{\kappa}] \\ [{}^{1}_{1}\boldsymbol{\kappa}] & [{}^{2}_{1}\boldsymbol{\kappa}] & [{}^{3}_{1}\boldsymbol{\kappa}] & [{}^{4}_{1}\boldsymbol{\kappa}] \\ [{}^{2}_{1}\boldsymbol{\kappa}] & [{}^{3}_{1}\boldsymbol{\kappa}] & [{}^{4}_{1}\boldsymbol{\kappa}] & [{}^{5}_{1}\boldsymbol{\kappa}] \\ [{}^{3}_{1}\boldsymbol{\kappa}] & [{}^{4}_{1}\boldsymbol{\kappa}] & [{}^{5}_{1}\boldsymbol{\kappa}] & [{}^{6}_{1}\boldsymbol{\kappa}] \end{matrix} & \mathbf{0}_{(8\times3)} \\ \mathbf{0}_{(3\times8)} & \begin{matrix} [{}^{0}_{2}\boldsymbol{\kappa}] & [{}^{1}_{2}\boldsymbol{\kappa}] & [{}^{2}_{2}\boldsymbol{\kappa}] \\ [{}^{1}_{2}\boldsymbol{\kappa}] & [{}^{2}_{2}\boldsymbol{\kappa}] & [{}^{3}_{2}\boldsymbol{\kappa}] \\ [{}^{2}_{2}\boldsymbol{\kappa}] & [{}^{3}_{2}\boldsymbol{\kappa}] & [{}^{4}_{2}\boldsymbol{\kappa}] \end{matrix} \end{bmatrix}, \tag{52}$$

and

$$\boldsymbol{\mathcal{E}}_{\boldsymbol{t}} = \left\{ {}^{0}_{1}\varphi\ {}^{0}_{2}\varphi\ {}^{1}_{1}\varphi\ {}^{1}_{2}\varphi\ {}^{2}_{1}\varphi\ {}^{2}_{2}\varphi\ {}^{3}_{1}\varphi\ {}^{3}_{2}\varphi\ {}^{0}_{3}\varphi\ {}^{1}_{3}\varphi\ {}^{2}_{3}\varphi \right\}^{\mathrm{T}}. \tag{53}$$

The first variation of the Green strain tensor components are

$$\begin{aligned} 2\delta{}^{0}_{\alpha\beta}\varepsilon &= \boldsymbol{r}_{,\alpha}\cdot\delta\bar{\mathrm{r}}_{,\beta} + \delta\boldsymbol{r}_{,\beta}\cdot\bar{\mathrm{r}}_{,\alpha}, \\ 2\delta{}^{1}_{\alpha\beta}\varepsilon &= \boldsymbol{r}_{,\alpha}\cdot\delta\bar{\mathrm{d}}_{,\beta} + \boldsymbol{r}_{,\beta}\cdot\delta\bar{\mathrm{d}}_{,\alpha} + \boldsymbol{d}_{,\alpha}\cdot\delta\bar{\mathrm{r}}_{,\beta} + + \boldsymbol{d}_{,\beta}\cdot\delta\bar{\mathrm{r}}_{,\alpha}, \\ 2\delta{}^{0}_{\alpha3}\varepsilon &= \boldsymbol{r}_{,\alpha}\cdot\delta\bar{\mathrm{d}} + \boldsymbol{d}\cdot\delta\bar{\mathrm{x}}_{,\alpha}. \end{aligned} \tag{54}$$

The position vector of the middle surface of the shell and the initial director vector are approximated as

$$\boldsymbol{r} = \sum_{I=1}^{4} \boldsymbol{N}_I \boldsymbol{r}_I, \quad \bar{\mathrm{r}} = \sum_{I=1}^{4} \boldsymbol{N}_I \bar{\mathrm{r}}_I, \tag{55}$$

$$\boldsymbol{d} = \sum_{I=1}^{4} \boldsymbol{N}_I \boldsymbol{d}_I, \tag{56}$$

where $\boldsymbol{N}_I$, $I = 1, 2, 3, 4$ are bilinear interpolation functions of the four-node element. The current director vector is interpolated as

$$\bar{\mathrm{d}} = \sum_{I=1}^{4} \boldsymbol{N}_I \bar{\mathrm{d}}_I, \tag{57}$$

where

$$\bar{\mathrm{d}}_I = \boldsymbol{\Lambda} \boldsymbol{d}_I, \tag{58}$$

and using the simplified Rodrigues' formula for small rotations (see [6,44]) one can get

$$\boldsymbol{\Lambda} = \boldsymbol{I} + \boldsymbol{W}, \tag{59}$$

where $\boldsymbol{W} = \text{skew}\, \boldsymbol{w}$ and $\boldsymbol{w}$ is the rotation vector. The variation of $\delta \bar{\mathrm{x}}_I = \delta \boldsymbol{v}_I$ with $\boldsymbol{v}_I$ denoting the displacement vector at each node and the variation of the director at each node is obtained as

$$\delta \bar{\mathrm{d}}_I = \boldsymbol{\Omega}^{\mathrm{T}} \delta \boldsymbol{w}_I, \tag{60}$$

$$\boldsymbol{\Omega} = \text{skew}\, \bar{\mathrm{d}}. \tag{61}$$

In finite element implementation at each node, by omitting the drilling rotation, defining local nodal rotations as $\boldsymbol{\beta}_I = \{\beta_1, \beta_2\}_I^{\mathrm{T}}$ and the local coordinate system $\boldsymbol{A} = [\bar{\mathrm{a}}_1, \bar{\mathrm{a}}_2]$ which can be tracked also by using the Rodrigues' formula in Eq. (59), one can obtain the virtual rotation vector $\delta \boldsymbol{w}_I$ as

$$\delta \boldsymbol{w}_I = \boldsymbol{A}\, \delta \boldsymbol{\beta}_I. \tag{62}$$

By using the bilinear interpolation of the position vector and of the director, the first variation of the strains can be described by

$$\{\delta \boldsymbol{\mathcal{E}}_{\boldsymbol{\varepsilon}}\} = \sum_{I=1}^{4} [\boldsymbol{B}_I^{\mathrm{v}}] \{\delta \mathbf{v}_I\}, \tag{63}$$

where the matrix $[\boldsymbol{B}]$ contains the derivatives of the bilinear interpolation and $\{\mathbf{v}_I\}^{\mathrm{T}} = \{\boldsymbol{v}_I, \boldsymbol{\beta}_I\}$. Following the same, the variation of the electric field, Eq. (30), can be expressed using numerical approximation as

$$\{\delta \boldsymbol{\mathcal{E}}_E\} = \sum_{I=1}^{4} \left[\boldsymbol{B}_I^{\phi}\right] \left\{\delta \boldsymbol{\phi}_I\right\}, \tag{64}$$

with $\{\boldsymbol{\phi}_I\}^{\mathrm{T}} = \{\overset{0}{\phi}_I, \overset{1}{\phi}_I, \overset{2}{\phi}_I\}$, and the variation of the temperature field with numerical approximation using Eq. (34) can be expressed as

$$\{\delta \boldsymbol{\mathcal{E}}_t\} = \sum_{I=1}^{4} \left[\boldsymbol{B}_I^{\vartheta}\right] \{\delta \boldsymbol{\vartheta}_I\}. \tag{65}$$

The enhanced strain field $\widetilde{\boldsymbol{\mathcal{E}}}_{\boldsymbol{\varepsilon}}$ can be obtained as

$$\{\widetilde{\boldsymbol{\mathcal{E}}}_{\boldsymbol{\varepsilon}}\} = \frac{|\boldsymbol{J}^0|}{|\boldsymbol{J}|} [\boldsymbol{N}_{\varepsilon}] \{\boldsymbol{\alpha}_{\varepsilon}\}, \tag{66}$$

where $[\boldsymbol{N}_{\varepsilon}]$ is an interpolation matrix with components $\{\boldsymbol{\alpha}_{\varepsilon}\}$, which appear as additional internal degrees of freedom, is given in Appendix B. The various matrices are $\boldsymbol{J}$ the Jacobian matrix, and $|\boldsymbol{J}^0|$ is the determinant of the Jacobian matrix at $\xi = 0$, $\eta = 0$. In this finite element 774 scheme is adopted and the matrices related to 774 scheme is defined in Appendix B.

3.1 The mass matrix

The inertia part related to the momentum balance law appears in Eq. (38), which contains the acceleration vector $\ddot{\boldsymbol{v}}$. By using the translational acceleration of the reference surface $\ddot{\bar{\mathrm{x}}}$ and the accelerative change of the director $\ddot{\bar{\mathrm{d}}}$, one can construct the acceleration vector $\ddot{\boldsymbol{v}}$ as

$$\ddot{\boldsymbol{v}} = \ddot{\bar{\mathrm{r}}} + z\ddot{\bar{\mathrm{d}}}. \tag{67}$$

By omitting the centripetal inertia forces and with the transformation matrix introduced in Eq. (60), one can express

$$\ddot{\bar{\mathrm{d}}}_I \approx \boldsymbol{\Omega}_I \ddot{\boldsymbol{\beta}}_{rI}. \tag{68}$$

The inertia term is given in the weak formulation Eq. (38) by a surface integral as

$$\int_V \boldsymbol{\rho}\, \ddot{\boldsymbol{v}} \cdot \delta\boldsymbol{v}\, \mathrm{d}V \approx \sum_{I=1}^{4}\sum_{K=1}^{4} \{\delta \mathbf{v}_I\}^{\mathrm{T}} [\boldsymbol{M}_{IK}] \{\ddot{\mathbf{v}}_K\}, \tag{69}$$

where

$$[\boldsymbol{M}_{IK}] = N_I \left[\begin{array}{c|c} \overset{0}{m}\, \boldsymbol{I}_{(3\times3)} & \overset{1}{m}\, \boldsymbol{\Omega}_K \\ \hline \overset{1}{m}\, \boldsymbol{\Omega}_I^{\mathrm{T}} & \overset{2}{m}\, \boldsymbol{\Omega}_I^{\mathrm{T}} \boldsymbol{\Omega}_K \end{array}\right] N_K, \tag{70}$$

with

$$\overset{n}{m} = \int_{\bar{z}}^{\tilde{z}} z^n\, \boldsymbol{\rho}\, \mathrm{d}z. \tag{71}$$

The static system of equations by incorporating interpolation functions to displacement and electric potentials for an element can be obtained as

$$\left[\begin{array}{ccc} \boldsymbol{M}_{\mathrm{uu}} & 0 & 0 \\ 0 & 0 & 0 \\ 0 & 0 & 0 \end{array}\right] \left\{\begin{array}{c} \Delta\mathbf{u} \\ \Delta\boldsymbol{\phi} \\ \Delta\boldsymbol{\alpha}_{\varepsilon} \end{array}\right\} + \left[\begin{array}{ccc} \boldsymbol{K}_{\mathrm{uu}} & \boldsymbol{K}_{\mathrm{u}\phi} + \boldsymbol{K}_{\mathrm{u}\phi}^{NL} & \boldsymbol{K}_{\mathrm{u}\tilde{\varepsilon}} \\ \boldsymbol{K}_{\phi\mathrm{u}} & \boldsymbol{K}_{\phi\phi} + \boldsymbol{K}_{\phi\phi}^{NL} & \boldsymbol{K}_{\phi\tilde{\varepsilon}} \\ \boldsymbol{K}_{\tilde{\varepsilon}\mathrm{u}} & \boldsymbol{K}_{\tilde{\varepsilon}\phi} + \boldsymbol{K}_{\tilde{\varepsilon}\phi}^{NL} & \boldsymbol{K}_{\tilde{\varepsilon}\tilde{\varepsilon}} \end{array}\right] \left\{\begin{array}{c} \Delta\mathbf{u} \\ \Delta\boldsymbol{\phi} \\ \Delta\boldsymbol{\alpha}_{\varepsilon} \end{array}\right\} = \left\{\begin{array}{c} \boldsymbol{F}_{\mathrm{u}} - \boldsymbol{F}_{\mathrm{u}}^{i} \\ \boldsymbol{F}_{\phi} - \boldsymbol{F}_{\phi}^{i} \\ -\boldsymbol{F}_{\alpha_{\varepsilon}}^{i} \end{array}\right\}, \tag{72}$$

$$[\boldsymbol{K}_{\vartheta\vartheta}] \left\{ \Delta\vartheta \right\} = \left\{ \boldsymbol{F}_{\vartheta} - \boldsymbol{F}_{\vartheta}^{i} \right\}, \tag{73}$$

where

$$\begin{aligned} \boldsymbol{K}_{\mathrm{uu}} &= \int_{\Omega} \boldsymbol{B}_{\mathrm{u}}^{\mathrm{T}} \mathbb{C}_{\boldsymbol{c}}\, \boldsymbol{B}_{\mathrm{u}}\, \mathrm{d}\Omega, \\ \boldsymbol{K}_{\mathrm{u}\phi} &= \boldsymbol{K}_{\phi\mathrm{u}}{}^{\mathrm{T}} = \int_{\Omega} \boldsymbol{B}_{\mathrm{u}}^{\mathrm{T}} \mathbb{C}_{\boldsymbol{e}}\, \boldsymbol{B}_{\phi}\, \mathrm{d}\Omega, \\ \boldsymbol{K}_{\mathrm{u}\tilde{\varepsilon}} &= \boldsymbol{K}_{\tilde{\varepsilon}\mathrm{u}}{}^{\mathrm{T}} = \int_{\Omega} \boldsymbol{B}_{\mathrm{u}}^{\mathrm{T}} \mathbb{C}_{\boldsymbol{c}}\, \boldsymbol{N}_{\tilde{\varepsilon}}\, \mathrm{d}\Omega, \\ \boldsymbol{K}_{\phi\tilde{\varepsilon}} &= \boldsymbol{K}_{\tilde{\varepsilon}\phi}{}^{\mathrm{T}} = \int_{\Omega} \boldsymbol{B}_{\phi}^{\mathrm{T}} \mathbb{C}_{\boldsymbol{e}}\, \boldsymbol{N}_{\tilde{\varepsilon}}\, \mathrm{d}\Omega, \\ \boldsymbol{K}_{\tilde{\varepsilon}\tilde{\varepsilon}} &= \int_{\Omega} \boldsymbol{N}_{\tilde{\varepsilon}}^{\mathrm{T}} \mathbb{C}_{\boldsymbol{c}}\, \boldsymbol{N}_{\tilde{\varepsilon}}\, \mathrm{d}\Omega, \\ \boldsymbol{K}_{\phi\phi} &= \int_{\Omega} \boldsymbol{B}_{\phi}^{\mathrm{T}} \mathbb{C}_{\boldsymbol{\epsilon}}\, \boldsymbol{B}_{\phi}\, \mathrm{d}\Omega \\ \boldsymbol{K}_{\vartheta\vartheta} &= \int_{\Omega} \boldsymbol{B}_{\vartheta}^{\mathrm{T}} \mathbb{C}_{\boldsymbol{\kappa}}\, \boldsymbol{B}_{\vartheta}\, \mathrm{d}\Omega \end{aligned} \tag{74}$$

are the element system matrices related to the constitutive relations. The nonlinear stiffness matrices at element level are

$$\begin{aligned} \boldsymbol{K}_{\mathrm{u}\phi}^{NL} &= \int_{\Omega} \boldsymbol{B}_{\mathrm{u}}^{\mathrm{T}} \mathbb{C}_{\boldsymbol{\beta}} \, \boldsymbol{B}_{\phi} \, \mathrm{d}\Omega, \\ \boldsymbol{K}_{\phi\phi}^{NL} &= \int_{\Omega} \boldsymbol{B}_{\phi}^{\mathrm{T}} \mathbb{C}_{\boldsymbol{\chi}} \, \boldsymbol{B}_{\phi} \, \mathrm{d}\Omega, \\ \boldsymbol{K}_{\tilde{\varepsilon}\phi}^{NL} &= \int_{\Omega} \boldsymbol{N}_{\tilde{\varepsilon}}^{\mathrm{T}} \mathbb{C}_{\boldsymbol{\beta}} \, \boldsymbol{B}_{\phi} \, \mathrm{d}\Omega. \end{aligned} \tag{75}$$

Here the generalised vector $\mathbf{u} = \{\mathbf{v}_1, \mathbf{v}_2, \mathbf{v}_3, \mathbf{v}_4\}^{\mathrm{T}}$ contains five mechanical DOFs per node, the generalised electric potential vector $\boldsymbol{\phi} = \{\boldsymbol{\phi}_1, \boldsymbol{\phi}_2, \boldsymbol{\phi}_3, \boldsymbol{\phi}_4\}^{\mathrm{T}}$ has three electrical DOFs per node and $\vartheta = \{\boldsymbol{\vartheta}_1, \boldsymbol{\vartheta}_2, \boldsymbol{\vartheta}_3, \boldsymbol{\vartheta}_4\}^{\mathrm{T}}$ has four thermal DOFs per node. In Appendix A, the matrices $\boldsymbol{B}_{\mathrm{u}}$ and $\boldsymbol{B}_{\phi}$ are given. Further, $\boldsymbol{F}_{\mathrm{u}}$ is the vector containing the mechanical loads, $\boldsymbol{F}_{\phi}$ is the electric load vector, $\boldsymbol{F}_{\mathrm{u}}^{i}$ is the vector containing in-balance forces, $\boldsymbol{F}_{\phi}^{i}$ is the in-balance electric load vector, $\boldsymbol{F}_{\vartheta}$ is the thermal load vector, $\boldsymbol{F}_{\vartheta}^{i}$ is the in-balance thermal forces and $\boldsymbol{F}_{\alpha_{\varepsilon}}$ is the in-balance force vector related to the enhanced parameters mentioned in Appendix B. For the thermal load problems considered in this article, the temperature difference at top and bottom surfaces are given. The distribution of temperature difference along the thickness is evaluated by solving Eq. (73), and this becomes input to the thermal strains in Eqs. (6) and (7). By making nonlinear terms zero in Eqs. (6) and (7), one can get the linear finite element model. The Newton–Raphson iteration and Newmark time integration techniques are used solve the static and dynamic problems, respectively.

4 Results and discussion

4.1 Validation

In this section, validation of the proposed numerical model is carried out by performing simulations on examples for which experimental data are available possessing nonlinear responses under strong applied electric fields. Two examples are considered, the first one is a bimorph plate actuator and the second one is a composite plate bonded with multiple piezopatches.

First, the bimorph plate actuator shown in Fig. 1 was studied experimentally by [22] and later with FE simulations by [18]. The plate dimensions are specified in Fig. 2. The bimorph actuator is fabricated using two PZT 3203 HD material layers with antiparallel polarisation direction configuration, where each PZT layer has a thickness of 0.25 mm. The material properties of the PZT 3203 HD are reported in Table 1. The problem is discretised with 120×25 elements. Since the developed shell element is based on equivalent single layer theory, only one element through the thickness is considered. The tip deflection of the plate is studied by performing static analysis using the present linear and materially nonlinear models. The tip deflection predicted by the

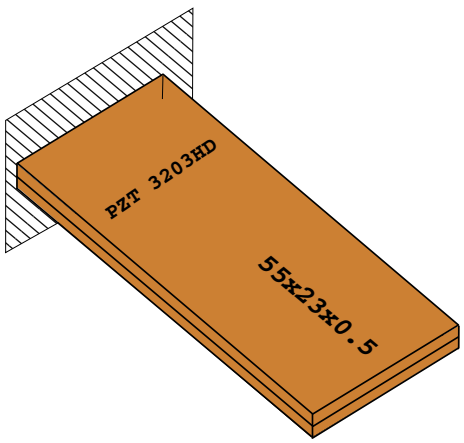

Fig. 2 Cantilevered bimorph plate actuator

Table 1 Material properties data

Property	Aluminium (Al)[b]	T300/976[a]	PZT 3203 HD[c]	PSI-5A-4E[d]	PZT-G1195[a]
E_{11} (10^9 N/m^2)	63.8	147.0	60.24	66.0	63.0
E_{22} (10^9 N/m^2)	63.8	9.7	60.24	66.0	63.0
G_{12} (10^9 N/m^2)	24.53	6.0	24.04	22.0	24.2
ν_{12} (10^9 N/m^2)	0.3	0.3	0.253	0.5	0.3
ν_{23} (10^9 N/m^2)	0.3	0.3	0.494	0.5	0.3
e_{31} (C/m^2)	0.0	0.0	−25.84	−25.08	−27.9
e_{32} (C/m^2)	0.0	0.0	−25.84	−25.08	−27.9
e_{15} (C/m^2)	0.0	0.0	24.04	12.84	14.15
e_{24} (C/m^2)	0.0	0.0	19.08	12.84	14.15
ϵ_{11} (10^{-9} F/m)	0.0	0.0	28.32	15.93	15.3
ϵ_{22} (10^{-9} F/m)	0.0	0.0	28.32	15.93	15.3
ϵ_{33} (10^{-9} F/m)	0.0	0.0	33.63	15.93	15.0
β_{31} (10^{-7} m^2/V^2)	0.0	0.0	520.0[e]	148.5[f]	148.5[f]
β_{32} (10^{-7} m^2/V^2)	0.0	0.0	520.0[e]	148.5[f]	148.5[f]
χ_3 (10^{-15} F/m)	0.0	0.0	0.0	0.0	80.0[g]
λ_{11} (10^5 N/m^{2}K)	–	0.721	–	–	5.45
λ_{22} (10^5 N/m^{2}K)	–	2.62	–	–	5.45
γ_{11} (10^{-3} C/m^{2}K)	–	–	–	–	0.25
γ_{22} (10^{-3} C/m^{2}K)	–	–	–	–	0.25
γ_{33} (10^{-3} C/m^{2}K)	–	–	–	–	0.25
κ_{11} (W/mK)	–	5.0	–	–	1.1
κ_{22} (W/mK)	–	0.5	–	–	1.1
κ_{33} (W/mK)	–	0.5	–	–	1.1

[a][35]
[b][10]
[c]Data available online at www.ctscorp.com/components/pzt/downloads/PiezoConstantMatrix.pdf
[d]Data available online at http://www.piezo.com
[e][17]
[f][49]
[g][24]

materially nonlinear FE model over the applied electric field is plotted in Fig. 3. For comparison purposes, the results from the experimental observations of [22] and also the numerical simulations of both linear and nonlinear FE models are shown in Fig. 3. As it can be seen from Fig. 3, the tip deflections predicted by the model are significantly nonlinear over the applied electric field. Furthermore, the present numerical simulations are compared with the numerical FE predictions of [18] in Fig. 3. From Fig. 3, it can be observed that the present simulations are in excellent agreement with the predictions of [18] and the better prediction capability is observed concerning experimental measurements of [22].

Next, a cantilevered composite plate bonded with multiple piezopatches is studied using the present numerical models. The geometry and the dimensions of the multi-piezoplate are shown in Fig. 4. Multiple piezopatches of PZT G1195 material are glued on either side of the graphite-epoxy T300/976 core composite with lamina sequence $(30_2/0)_s$. The material properties of the composite and piezoelectrics are given in Table 1. The multi-piezopatch problem was first studied experimentally by [4]. Here also one element through the thickness is considered as described in the previous example.

An electric field of 472 V/mm is applied on either side of the piezolayers with opposite polarity to examine the response of the plate. Following [4], the responses are plotted in non-dimensional displacements as bending (w_2/L_2) and twisting $((w_3 - w_1)/L_2)$ over the length (L) of the plate in Fig. 5, where L_2 is the width of the plate while w_1, w_3, and w_2 are the transverse deflections in the corners 1, 3, and at the centre line 2 as shown in Fig. 4, respectively. From the observations in Fig. 5, it can be seen that the present materially nonlinear FE simulations predict the behaviour closer to the experimental results of [4], whereas the linear FE model predicts stiffer response when compared to the experimental observations and nonlinear simulations. Considering the above two examples as validation, it can be concluded that the nonlinear model analysis results predict the actual response of piezolaminated structures more faithfully.

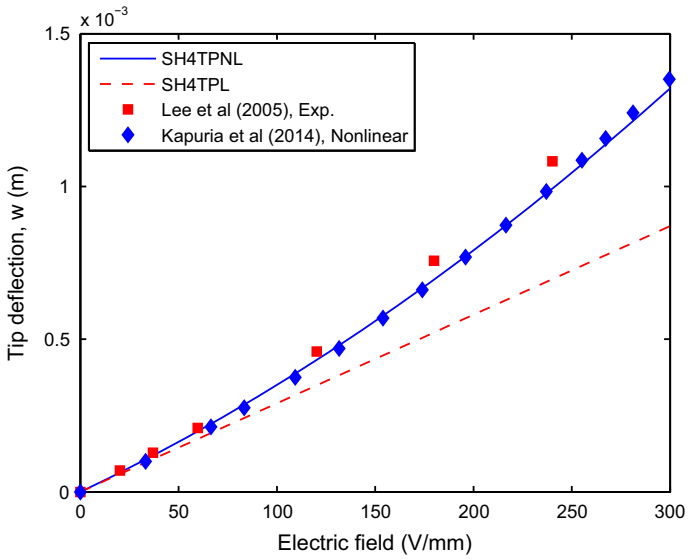

Fig. 3 Tip deflection versus electric field

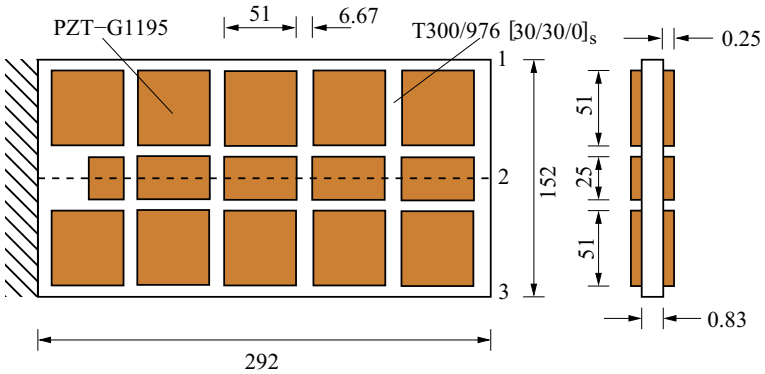

Fig. 4 Cantilevered composite plate with multiple piezopatches

4.2 Active shape control of plates and shells

4.2.1 Shape control of a plate under thermal/elastic loads

A simply supported square composite plate (0.2×0.2 m) with piezolaminated layers is shown in Fig. 6. The host structure is fabricated from T300/976 graphite-epoxy with $[45/-45/-45/45]$ laminate configuration. It is bonded with two outer layers of PZT G1195 material. Each composite layer has a thickness of 0.5 mm, and each piezoelectric layer has a thickness of 0.1 mm. Thus, the total thickness of the structure is 2.2 mm. The material properties of the graphite-epoxy and those of the PZT are listed in Table 1. Here the aim of the simulation is shape control of the plate structure under thermal gradient loading via PZT layers. To do so, a double sinusoidal temperature difference of 40 K $\sin(\pi x/L)\sin(\pi y/L)$ is enforced at the top surface of the plate with respect to the stress-free temperature 293 K, and the lower surface of the plate is kept at stress-free temperature.

By applying appropriate voltages, the shape control of the plate is simulated. Both linear and materially nonlinear simulations are performed to revert the midpoint deflection of the plate. Figure 7 shows the linear and nonlinear deflections of the centre line of the plate under different applied actuator voltages to top and bottom surfaces. On the other hand, Table 2 summarises the required voltages using both linear and nonlinear FE models to suppress the centre deflection to the extent of 100, 80, 60, 20% of the uncontrolled deflection under the temperature gradient. From Table 2, it is clearly seen that the linear model predicts higher values of the required actuator voltages for deflection control when compared to the nonlinear model. With the increase

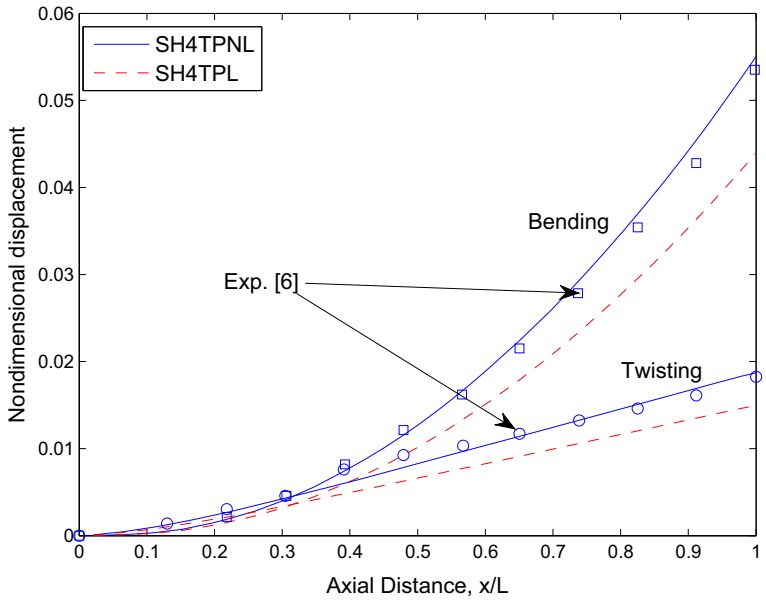

Fig. 5 Non-dimensional deflection of the cantilevered plate bonded with multiple piezopatches under actuation field of 472 V/mm

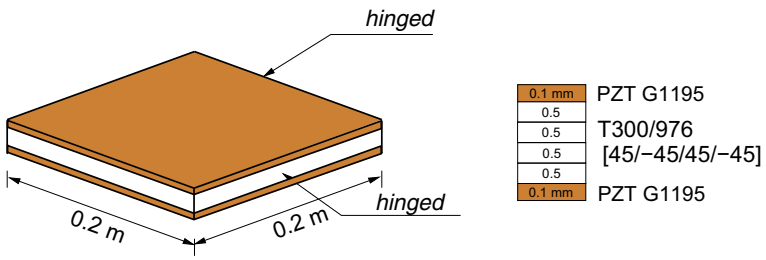

Fig. 6 Piezolaminated composite plate

in the decline of the central deflection, the difference between the linear and nonlinear predictions of actuator voltages also increases. This phenomenon occurs because of the large applied voltages required to control the higher amount of deflection. Thus, those large applied voltages induce a greater degree of piezoelectric nonlinearity.

A set of computations is performed with the same example by varying the piezoelectric layer thickness values. The host layer is the same as in the previous study. The piezoelectric layer thickness ranges from 0.05 to 0.2 mm. Here the temperature difference at the top surface is the same as for the problem mentioned above, i.e. double sinusoidal along the in-plane dimensions of the plate, with magnitude 40 K at the plate centre. Figure 8 illustrates the effect of piezoelectric thickness over the control voltages of the piezolaminated composite plate. Using both linear and materially nonlinear models, the prediction of actuation voltages to control the centre deflection to zero is plotted as a function of 10 (h_p/h_c) in Fig. 8. As the thickness of the PZT decreases, the thermal stresses also decrease resulting in both linear and nonlinear control voltages decrease. The %-difference between linear and nonlinear FE models is plotted as a function of PZT thickness 10 (h_p/h_c) in Fig. 9. From Fig. 9, it can be observed that the %-difference varies nonlinearly over the thickness of the PZT layer. In a similar manner, some more computations are carried out with the same example by varying the piezoelectric layer thickness values under a point load of 100 N at the plate centre. The host layer is the same as in the previous study but with a different dimension of the host structure thickness which is 3 mm for the present study. The shape control problem is as described above analysed here also. Figure 10 represents linear and nonlinear control voltages required to suppress 80% of centre deflection of the plate under point load. One can observe from Fig. 10 that the control voltages needed for the same amount of the point load in linear case increase as the PZT thickness decreases. This behaviour is due to the fact that for lesser thickness of the PZT one can observe larger deflections of the plate since the stiffness of the whole structure decreases. However,

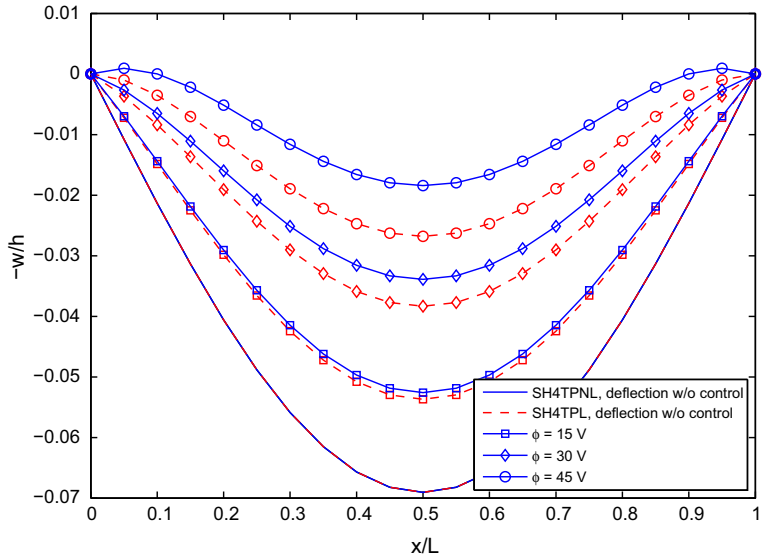

Fig. 7 Centre line deflection of the plate under thermal loading at the top surface of the plate

Table 2 Tip deflections over applied voltage

%-Reduction of the centre deflection	Voltage		
	SH4TPL	SH4TPNL	% difference
20	13.486	12.690	5.89
40	26.970	24.153	10.44
60	40.453	34.656	14.33
80	53.938	44.423	17.64
100	67.420	53.580	20.05

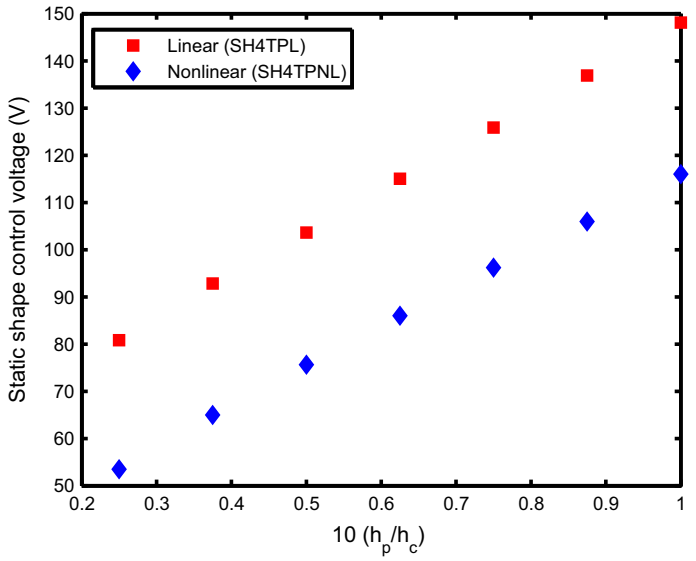

Fig. 8 Actuation voltage variation for different piezoelectric layer thickness under temperature gradient

lower values of control voltages are predicted by the nonlinear model (see Fig. 10). One can easily explain the reason for this behaviour as the consequence of lower PZT thickness values leading to higher electric fields; thus, the nonlinear effect is also higher. Figure 11 shows the %-difference between linear and nonlinear FE models plotted as a function of PZT thickness 10 (h_p/h_c) under point load.

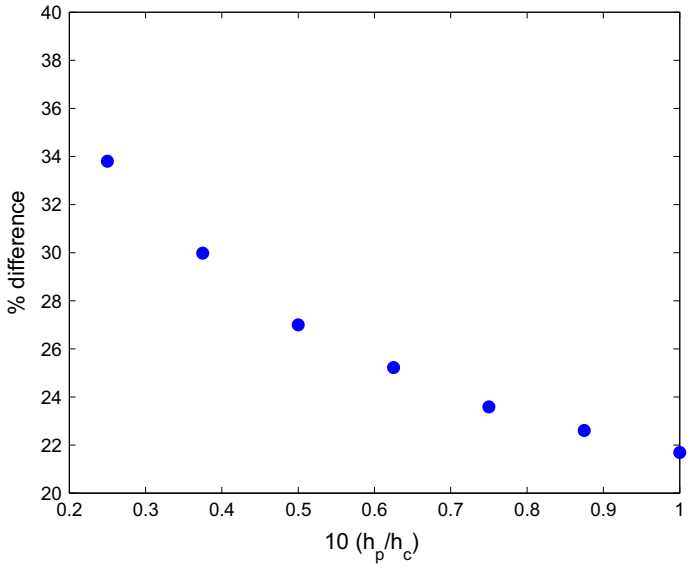

Fig. 9 %-Difference between linear and nonlinear predictions of actuation voltage under thermal load

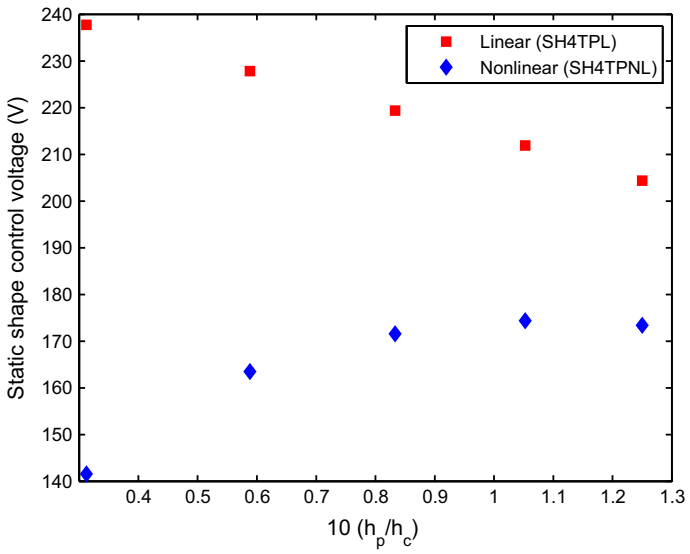

Fig. 10 Actuation voltage variation for different piezoelectric layer thickness under point load at the centre of the plate

4.2.2 Shaping of a spherical antenna reflector via PZT patches

In this section, a spherical antenna reflector laminated with piezoelectric patches (see Fig. 12) is considered. This example was initially studied by [10] with experimental observations. The geometric parameters of the shell and the patches are shown in Fig. 12, radius ("R") of 203 mm, and semi-aperture angle "θ" of 45°. The piezopatches have the length "l" of 36 mm and are located at a distance "a" of 50 mm from the 2° angle in the middle. The host substrate is made up of isotropic material (aluminium) and has a thickness of 0.36 mm. The PSI 5A piezopatches have a thickness of 0.267 mm. At the inner hole, clamped boundary conditions are enforced and also the displacements in the vertical direction are fixed.

This type of spherical antennas with PZT patches have properties like manoeuvrability, beam steering and shaping. Alteration of the area from one position to another position is called beam steering, while shaping is the phenomenon of increasing or decreasing the area covered/radiation pattern around the principle direction. Here, the goal is shaping of the spherical antenna reflector which can be achieved by inducing a strain by application of an electric field to the piezopatches.

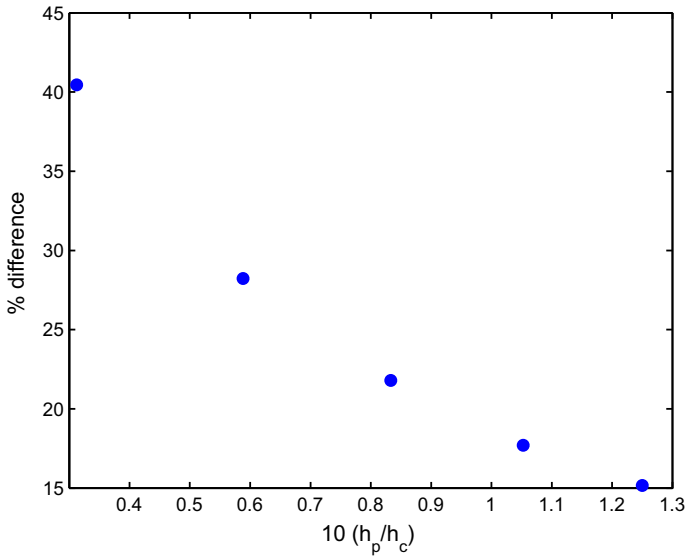

Fig. 11 %-Difference between linear and nonlinear predictions of actuation voltage under point load at the centre of the plate

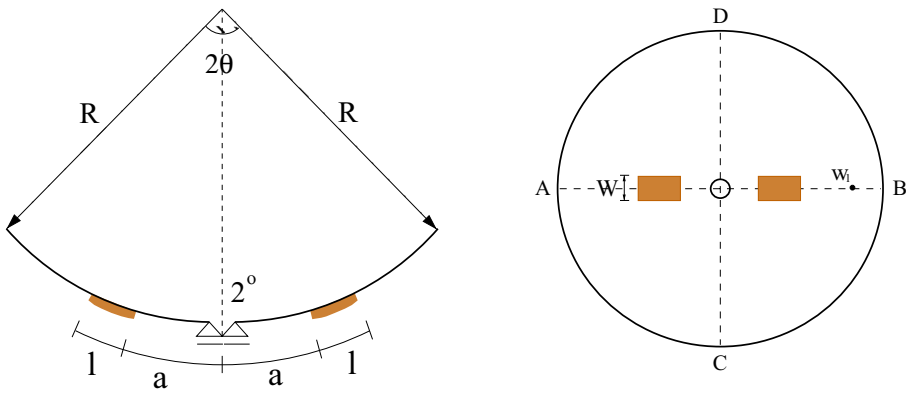

Fig. 12 Spherical antenna reflector with PZT actuator patches

Table 3 Transverse deflection at point "1": w_1 over applied voltage

Voltage (V)	Transverse deflection at point "1": w_1 (μm)			
	SH4TPL	SH4TPNL	Exp. [10]	Error
14.5	7.34	7.46	8.03	7.09
29.5	14.94	15.50	16.98	8.76
43	21.78	22.51	25.30	11.02
62	31.40	32.50	34.76	6.50
74.5	37.73	39.00	41.30	5.57
90.5	45.83	48.00	50.25	4.48

At first, the deflection at point "1", i.e. (w_1), which is 50 mm from the apex outer side (see Fig. 12) is simulated with both linear and nonlinear constitutive models by applying the actuation voltage of 100 V to the both PSI 5A patches. The material properties of PSI-5A are reported in Table 1.

The w_1 displacements predicted by the SH4TPL and SH4TPNL along with experimental measurements of [10] are summarised in Table 3. From Table 3, it is noticed that once again results predicted by the SH4TPNL model are better than by linear models concerning the experiments of [10]. The %-error of nonlinear predictions regarding the experiments is also given in Table 3. However, the discrepancies between the experiments and our nonlinear models are because the experiments were conducted on the imperfect shell (imperfections arise

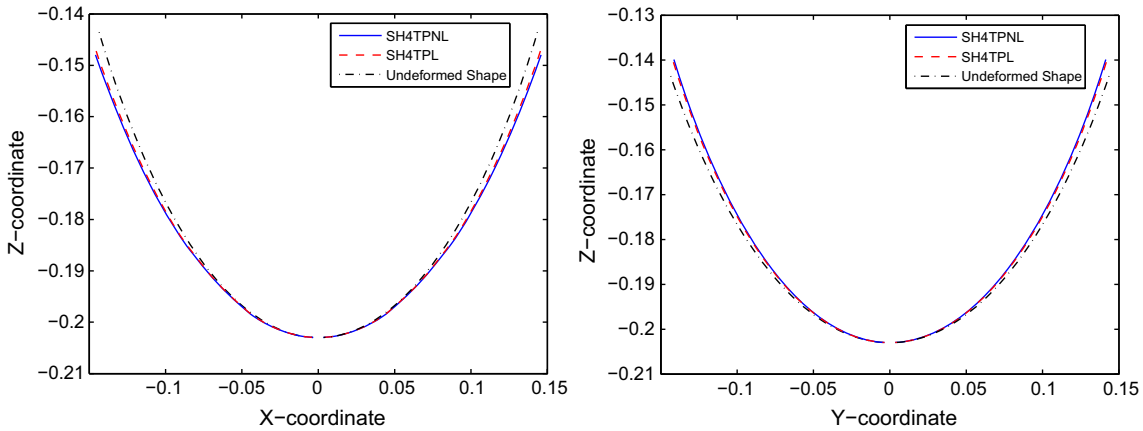

Fig. 13 Shaping of antenna: left, deflection along the line AB; right, deflection along the line CD (scaled $10\times$ w)

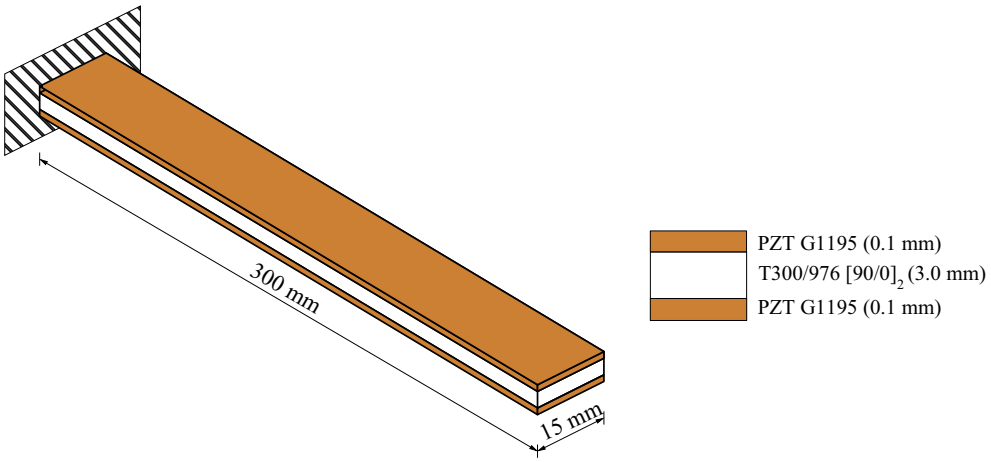

Fig. 14 Cantilevered composite beam with PZT layers

due to the fabrication process like wrinkles). In the next study, the shaping of the spherical antenna reflector is performed by enforcing the actuation voltage of 140 V to each piezopatch. Deflections along the line AB and CD are plotted in Fig. 13. In satellite antennas usually high precision is required to change the radiation pattern. Thus, using nonlinear PZT modelling alteration of the radiation can be achieved more precisely.

4.3 Active vibration control of piezolaminated shells

In the aforementioned subsections, it was shown how the nonlinear SH4TPNL model can be used to control the static deflections under mechanical/thermal loads. We also have demonstrated the predicting capabilities of SH4TPNL and SH4TPL models in earlier sections, and now continue to display the potentiality of the nonlinear model (SH4TPNL) over the linear model (SH4TPL) in dynamics and vibration suppression.

4.3.1 Vibration control of a beam with PZT layers at temperature gradient

The problem studied here is the active vibration control of a cantilevered composite beam as shown in Fig. 14. Two PZT layers are bonded on either side of the host surface. The material properties of the T300/976 and PZT G1195 are listed in Table 1. The temperature difference of 20° C and 10° C are applied to the lower and upper surfaces, respectively. The stress-free temperature is taken as 10° C. The problem is discretised with a mesh of size [20 × 4] elements.

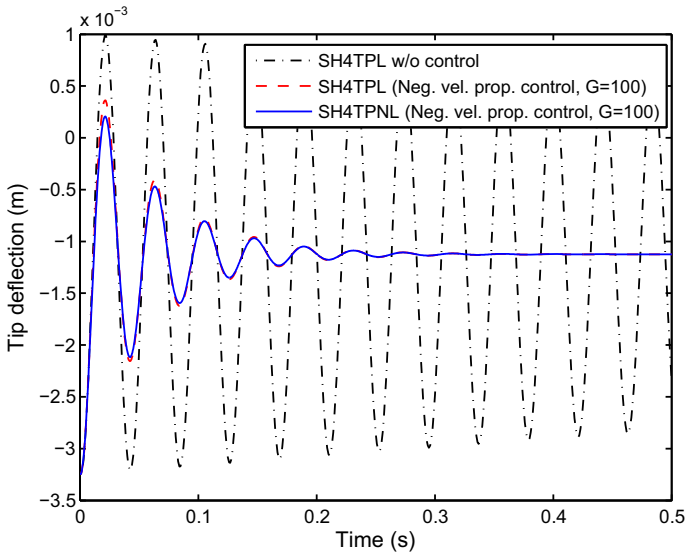

Fig. 15 Uncontrolled and controlled tip deflections at temperature load

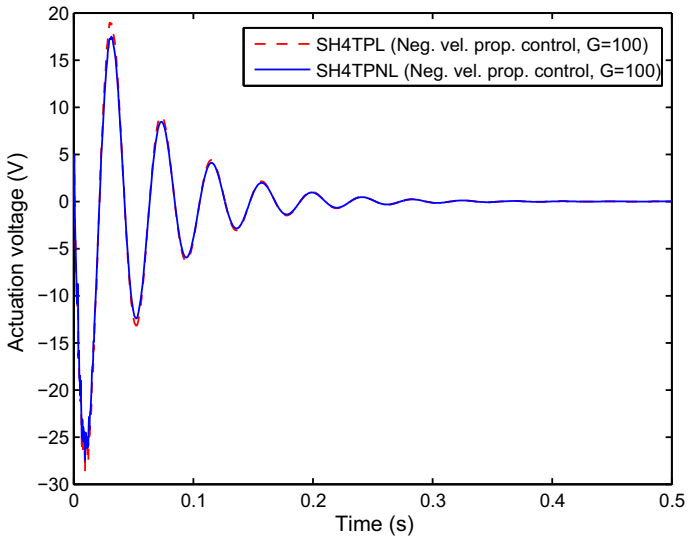

Fig. 16 Actuation voltages over time

The transient response of the problem is studied by imposing an initial transverse displacement of 28 mm at the free end of the beam, and the beam oscillates afterwards freely. The initial displacement is chosen such that the deformation of the structure does not exceed the thickness of the complete structure. The Newmark method with a time step of 1×10^{-4} s is considered with Rayleigh damping of 0.2%. First, the response is simulated without any feedback control, and the tip deflection is shown in Fig. 15. Next, the control voltages are applied to both piezolayers in opposite directions using a negative velocity feedback technique as $V = G \cdot \dot{u}_{n,\text{tip}}$. Here, the gain $G = 500$ Vs/m is applied and $\dot{u}_{n,\text{tip}}$ is the tip normal velocity. The controlled response simulated by both SH4TPL and SH4TPL along with uncontrolled tip deflections are shown in Fig. 15. Figure 16 illustrates the actuation voltages required to suppress the deformations by linear and materially nonlinear models. However, the controlled response of the structure is staying at the deformation corresponding to the bending moments generated due to the temperature difference on top and lower surfaces. To get back the structure into the zero displacement conditions an electric voltage proportional to the static deflection which is due to the temperature difference is applied additionally along with the negative velocity feedback control.

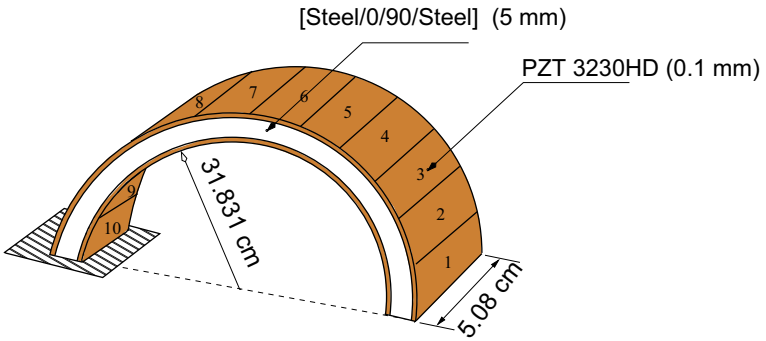

Fig. 17 Cantilevered composite cylindrical shell with PZT patches as distributed layers

4.3.2 Smart cantilevered fibre metal-laminated composite cylindrical shell

The last numerical example considered here is the cantilevered fibre metal-laminated composite cylindrical shell as shown in Fig. 17. Tzou and Ye initially calculated the isotropic version of this problem [42] for active control of small amplitude vibrations using linear piezoelectric constitutive relations. Later by [3,32], this problem has been used for suppression of geometrically nonlinear vibrations. The host structure consists of fibre metal composite of steel/0/90/steel with each layer thickness of 1.25 mm and piezoelectric PZT 3203 HD material in either layer or patch forms bonded to both sides of the shell. The thickness of the PZT 3203 HD material is 0.1 mm. The inner PZT layer/patches serve as the sensors, and the external ones as actuators. The material properties of the steel, T300/976 and PZT 3203 HD, are listed in Table 1. Here, simulations are performed to observe the uncontrolled transient response of the structure under impact loading by applying dynamic load configurations as

$$P(t) = \begin{cases} (P_t \cdot t)/0.01 & \text{if } t \leq 0.01 \text{ s}, \\ P_t & \text{if } 0.01 \text{ s} \leq t \leq 0.19 \text{ s}, \\ P_t - (P_t \cdot t/0.2) & \text{if } 0.19 \text{ s} \leq t \leq 0.2 \text{ s}, \\ 0 & \text{else}, \end{cases} \tag{76}$$

along with 0.2% Rayleigh damping for each mode without considering the continuous PZT layers.

Next, the active vibration control of the cylindrical shell is performed by continuous PZT actuator–sensor layers using negative velocity feedback control algorithm. First, $\dot{u}_{n,\text{avg}}$, the average of normal velocities are calculated in the centre points of piezopatches of the sensor layer and then a voltage proportional to the average normal velocity $V = G \cdot \dot{u}_{n,\text{avg}}$, with the gain $G = 2000$ Vs/m, is applied. For 100% covered actuator–sensor patches (i.e. distributed layers), the controlled response of the structure simulated by SH4TPNL and SH4TPL models is illustrated in Figs. 18a, b. Figure 18c shows the predicted actuator voltages over time with linear and materially nonlinear models. From Figs. 18a, b, it can be observed that the decay of vibration amplitude estimated by the SH4TPL model is larger compared to the nonlinear SH4TPL model. In Fig. 18d, the deformed configurations at various time instants are presented.

Next, the same study is performed with 50% covered by piezopatches from the fixed end (i.e. five patches) as shown in Fig. 19. The simulated linear and nonlinear controlled responses along with the deformed configurations at different time instants are shown in Fig. 20. The control effect is more time-consuming for a fixed ratio of suppression of vibration amplitude when compared to the structure is 100% covered by piezoelectric sensor and actuator layers.

Furthermore, the structure is treated when 50% are covered with patches from the free end (see Fig. 21). The tangential and normal deflections of the tip are shown in Figs. 22 and 23, respectively. It can be observed that the control effect is very small for both the linear model and nonlinear models. By examining the two problems of 50 % covered patches together, one can notice that the decay of vibrations is larger in the first case compared to the second case.

5 Conclusions

In this article, a two-way coupled nonlinear piezoelectric finite element for shape control and vibration suppression analysis of multilayered composite plates/shells are presented. Second-order approximation of the

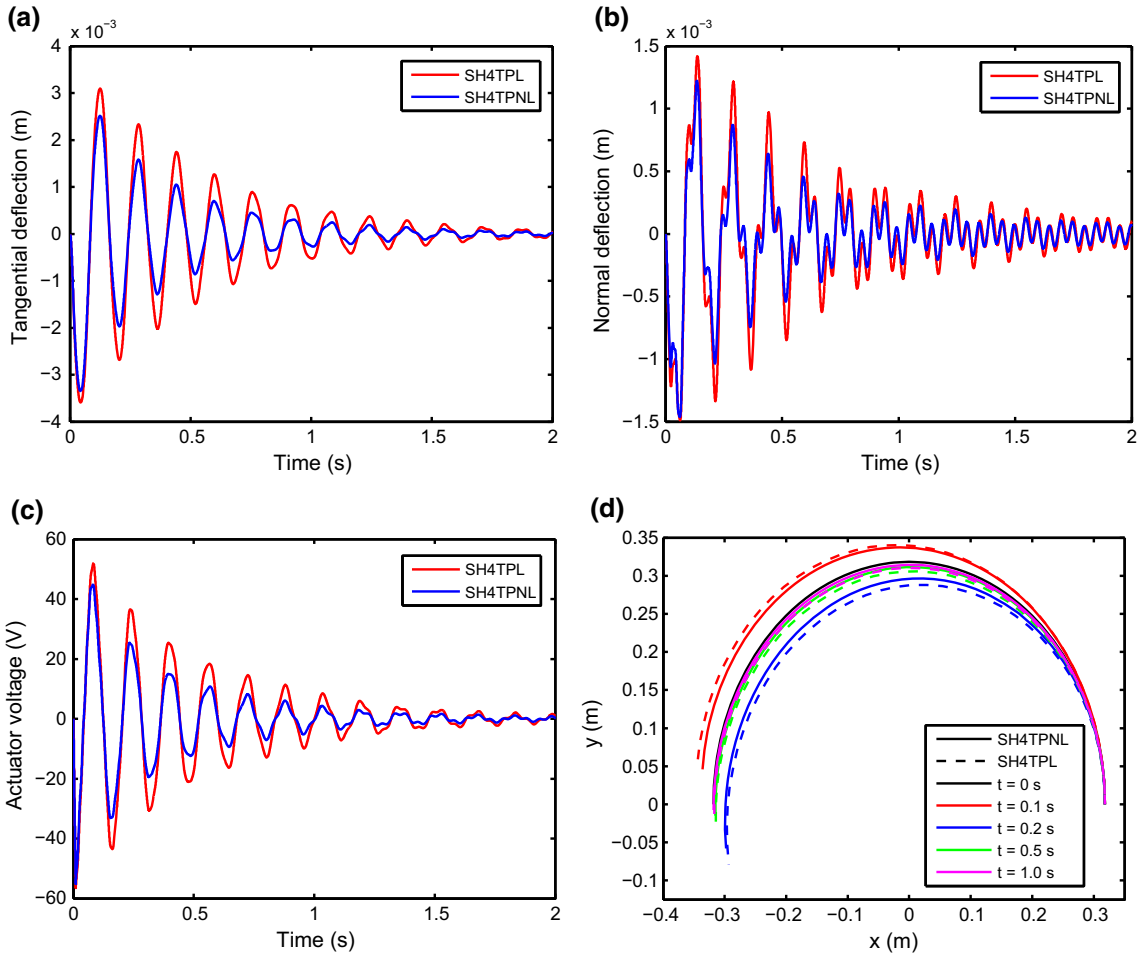

Fig. 18 Controlled and uncontrolled response of composite cylindrical shell covered with 100% PZT patches: **a** tangential deflection, **b** normal deflection, **c** actuator voltages and **d** deformed configurations

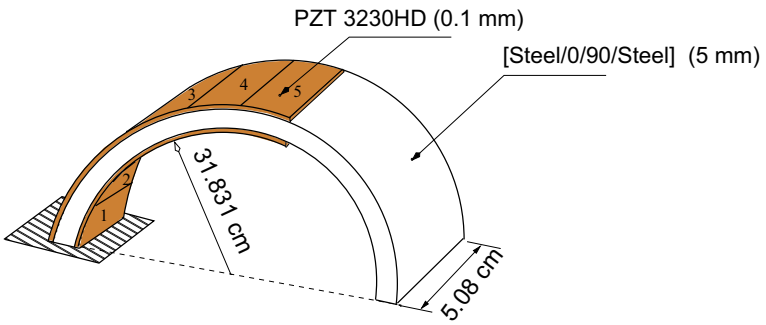

Fig. 19 Cantilevered composite cylindrical shell with 50% covered by PZT patches from fixed end

electric potential over the thickness is assumed. ANS and EAS methods are used to enrich the strain fields of FE element. Third-order approximation is used for the temperature difference distribution along the thickness, and one-dimensional heat conduction equation is solved in equivalent single-layer hypothesis. The potentiality and effectiveness of the SH4TPNL/SH4TPL elements is demonstrated with several examples. A bimorph plate and a composite plate with bonded piezopatches are considered to validate the numerical simulations. The given examples in this paper contribute to benchmark problems of future works, and in conclusion, predictive capabilities of the proposed numerical model under strong electric fields are illustrated with a wide variety of

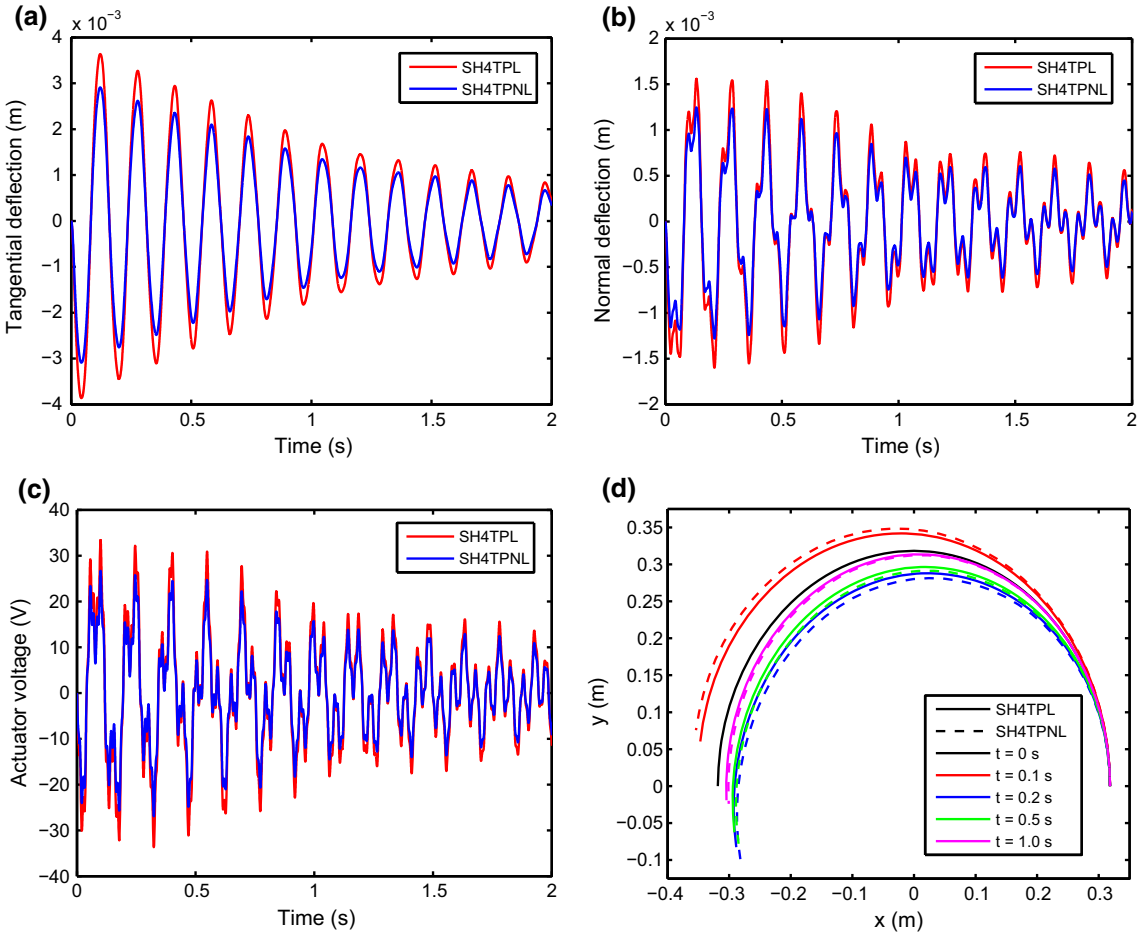

Fig. 20 Controlled and uncontrolled response of composite cylindrical shell covered with 50% PZT patches from the fixed end: **a** tangential deflection, **b** normal deflection, **c** actuator voltages and **d** deformed configurations

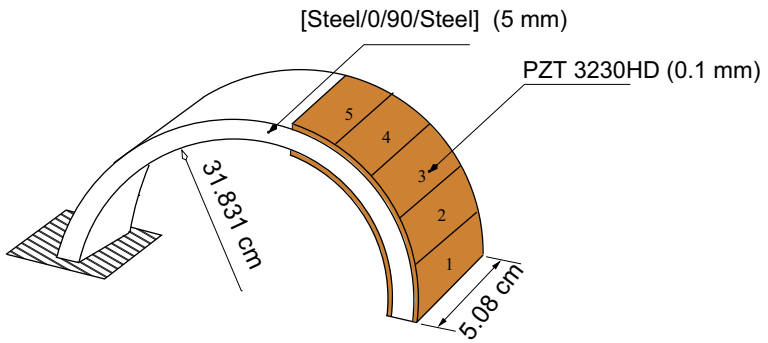

Fig. 21 Cantilevered composite cylindrical shell with 50% covered by PZT patches from free end

smart structures numerical examples. Shape control of laminated plate with piezoelectric active layers under both thermal and mechanical load environments are performed using the linear and nonlinear models to highlight predictive capabilities as well as the difference of required actuator voltages. Additionally, shaping of a spherical shell antenna reflector is also discussed. A cantilevered beam with PZT layers under temperature gradient is considered to show the effects of nonlinear terms of the constitutive relations in vibration suppression analysis. Furthermore, three different arrangements of piezopatches are deemed to illustrate the effect of position of piezoelectrics in cantilevered cylindrical shells to control vibrations under impulsive force at the free end of the shell.

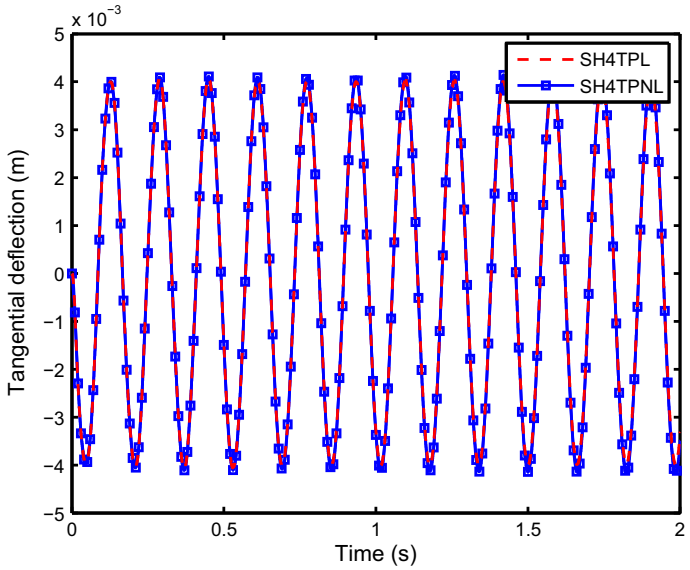

Fig. 22 Controlled tangential deflection, 50% patches from free end

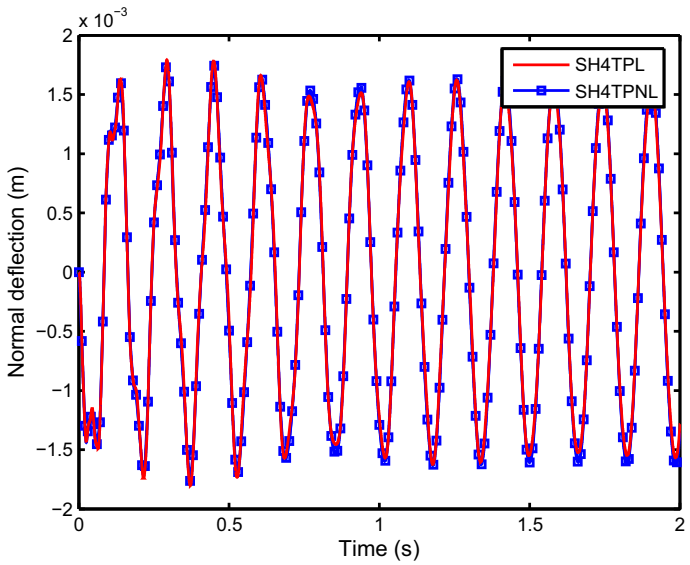

Fig. 23 Controlled normal deflection, 50% patches from free end

In particular, stress softening behaviour under large applied electric fields of PZT actuators cannot be estimated with the linear constitutive models. Therefore, it is essential to adopt the advanced finite element formulations for the precise prediction of actuator response and also for the design of PZT structures with higher authority of actuation. It was justified with the proposed nonlinear constitutive piezo shell finite element to predict the actual responses since the analysis results are better estimated from the viewpoint of experimental data. Hence it is confirmed that the developed element could be a useful tool for predicting actual responses in both static and dynamics.

Large applied electric voltages result in higher actuation and lead to more substantial shape control attainment. However, increasing the thickness of PZT actuators results in lower applied electric fields across the thickness of the actuators and also the stiffness against bending deformation enhances. The effect of piezoelectric nonlinearity has a significant influence on the performance of the PZT actuators in the active shape control phenomenon. In this manner, the optimal shape control of laminated structures can be accomplished

by choosing suitable actuators regarding the size and shape of elastic/electrical (either linear or nonlinear) properties.

The size and position where the actuators are mounted also alters the performance of the active vibration control of smart structures. Usually, actuators in the form of layers have higher authority actuation area causing better control of vibrations when compared with the actuator patches. Furthermore, actuator patches situated proximate to the fixed/clamped ends have more vibration control performance, while their competence to suppress the vibrations decreases substantially when placed far from the fixed end.

Appendix A: Various rigidity matrices

The following abbreviations have been used:

$$[\overset{n}{\boldsymbol{C}}_i] = \int_{\bar{z}}^{\bar{\bar{z}}} z^n [\boldsymbol{C}_i]\, \mathrm{d}z, \tag{A.1}$$

$$[\overset{n}{\boldsymbol{\lambda}}_1] = \int_{\bar{z}}^{\bar{\bar{z}}} z^n [\boldsymbol{\lambda}_1]\, \mathrm{d}z, \tag{A.2}$$

$$[\overset{n}{\boldsymbol{e}}_i] = -\int_{\bar{z}}^{\bar{\bar{z}}} z^n [\boldsymbol{e}_i]\, \mathrm{d}z, \tag{A.3}$$

$$[\overset{n}{\boldsymbol{\epsilon}}_i] = -\int_{\bar{z}}^{\bar{\bar{z}}} z^n [\boldsymbol{\epsilon}_i]\, \mathrm{d}z, \tag{A.4}$$

$$[\overset{n}{\boldsymbol{\beta}}_1] = -\int_{\bar{z}}^{\bar{\bar{z}}} \left(z^n [\boldsymbol{\beta}_1]\, \Delta\, \overset{1}{\phi} + z^{n+1} [\boldsymbol{\beta}_1]\, \Delta\, \overset{2}{\phi} \right) \mathrm{d}z, \tag{A.5}$$

$$[\overset{n}{\boldsymbol{\gamma}}_1] = \int_{\bar{z}}^{\bar{\bar{z}}} z^n [\boldsymbol{\gamma}_1]\, \mathrm{d}z, \tag{A.6}$$

$$[\overset{n}{\boldsymbol{\chi}}_1] = -\int_{\bar{z}}^{\bar{\bar{z}}} \left(z^n [\boldsymbol{\chi}_1]\, \Delta\, \overset{1}{\phi} + z^{n+1} [\boldsymbol{\chi}_1]\, \Delta\, \overset{2}{\phi} \right) \mathrm{d}z, \tag{A.7}$$

$$[\overset{n}{\boldsymbol{\kappa}}_i] = \int_{\bar{z}}^{\bar{\bar{z}}} z^n [\boldsymbol{\kappa}_i]\, \mathrm{d}z, \tag{A.8}$$

$$\boldsymbol{L}^{\vartheta} = \begin{bmatrix} \frac{(3\,\bar{z} - \overset{+}{z})\,\overset{+}{z}^2}{k_1} & \frac{(\bar{z} - 3\,\overset{+}{z})\,\bar{z}^2}{k_1} & -\frac{\bar{z}\,\overset{+}{z}^2}{k_2} & -\frac{\bar{z}^2\,\overset{+}{z}}{k_2} \\ -\frac{6\,\bar{z}\,\overset{+}{z}}{k_1} & \frac{6\,\bar{z}\,\overset{+}{z}}{k_1} & \frac{(2\,\bar{z} + \overset{+}{z})\,\overset{+}{z}}{k_2} & \frac{(\bar{z} + 2\,\overset{+}{z})\,\bar{z}}{k_2} \\ \frac{3(\bar{z} + \overset{+}{z})}{k_1} & -\frac{3(\bar{z} + \overset{+}{z})}{k_1} & -\frac{(\bar{z} + 2\,\overset{+}{z})}{k_2} & -\frac{(2\,\bar{z} + \overset{+}{z})}{k_2} \\ -\frac{2}{k_1} & \frac{2}{k_1} & \frac{1}{k_2} & \frac{1}{k_2} \end{bmatrix}, \tag{A.9}$$

with

$$k_1 = (\bar{z} - \overset{+}{z})^3 \quad \text{and} \quad k_2 = (\bar{z} - \overset{+}{z})^2. \tag{A.10}$$

The matrices in Eq. (74) are

$$\boldsymbol{B}_{\mathrm{u}} = \{\boldsymbol{B}_1^{\mathrm{v}}, \boldsymbol{B}_2^{\mathrm{v}}, \boldsymbol{B}_3^{\mathrm{v}}, \boldsymbol{B}_4^{\mathrm{v}}\}, \tag{A.11}$$

$$\boldsymbol{B}_{\phi} = \{\boldsymbol{B}_1^{\phi}, \boldsymbol{B}_2^{\phi}, \boldsymbol{B}_3^{\phi}, \boldsymbol{B}_4^{\phi}\}, \tag{A.12}$$

$$\boldsymbol{B}_{\vartheta} = \{\boldsymbol{B}_1^{\vartheta}, \boldsymbol{B}_2^{\vartheta}, \boldsymbol{B}_3^{\vartheta}, \boldsymbol{B}_4^{\vartheta}\}. \tag{A.13}$$

Appendix B: Interpolation functions for EAS method

The 774 scheme in the EAS (i.e. 18 additional internal DOFs) for the strain field is constructed by using the following matrices:

$$\boldsymbol{N}_{\tilde{\varepsilon}} = \boldsymbol{T}_{\tilde{\varepsilon}}^{-1} \boldsymbol{M}_{\tilde{\varepsilon}}, \tag{B.1}$$

with

$$\boldsymbol{T}_{\tilde{\varepsilon}} = \begin{bmatrix} J_{11}^0 J_{11}^0 & J_{12}^0 J_{12}^0 & J_{11}^0 J_{12}^0 & 0 & 0 & 0 & 0 & 0 \\ J_{21}^0 J_{21}^0 & J_{22}^0 J_{22}^0 & J_{21}^0 J_{22}^0 & 0 & 0 & 0 & 0 & 0 \\ 2J_{11}^0 J_{21}^0 & 2J_{12}^0 J_{22}^0 & J_{11}^0 J_{22}^0 + J_{12}^0 J_{21}^0 & 0 & 0 & 0 & 0 & 0 \\ 0 & 0 & 0 & J_{11}^0 J_{11}^0 & J_{12}^0 J_{12}^0 & J_{11}^0 J_{12}^0 & 0 & 0 \\ 0 & 0 & 0 & J_{21}^0 J_{21}^0 & J_{22}^0 J_{22}^0 & J_{21}^0 J_{22}^0 & 0 & 0 \\ 0 & 0 & 0 & 2J_{11}^0 J_{21}^0 & 2J_{12}^0 J_{22}^0 & J_{11}^0 J_{22}^0 + J_{12}^0 J_{21}^0 & 0 & 0 \\ 0 & 0 & 0 & 0 & 0 & 0 & J_{11}^0 & J_{12}^0 \\ 0 & 0 & 0 & 0 & 0 & 0 & J_{21}^0 & J_{22}^0 \end{bmatrix} \tag{B.2}$$

and

$$\boldsymbol{M}_{\tilde{\varepsilon}} = \begin{bmatrix} \xi & 0 & \xi\eta & 0 & 0 & 0 & 0 & 0 & 0 & 0 & 0 & 0 & 0 & 0 & 0 & 0 & 0 & 0 \\ 0 & \eta & 0 & \xi\eta & 0 & 0 & 0 & 0 & 0 & 0 & 0 & 0 & 0 & 0 & 0 & 0 & 0 & 0 \\ 0 & 0 & 0 & 0 & \xi & \eta & \xi\eta & 0 & 0 & 0 & 0 & 0 & 0 & 0 & 0 & 0 & 0 & 0 \\ 0 & 0 & 0 & 0 & 0 & 0 & \xi & 0 & \xi\eta & 0 & 0 & 0 & 0 & 0 & 0 & 0 & 0 & 0 \\ 0 & 0 & 0 & 0 & 0 & 0 & 0 & \eta & 0 & \xi\eta & 0 & 0 & 0 & 0 & 0 & 0 & 0 & 0 \\ 0 & 0 & 0 & 0 & 0 & 0 & 0 & 0 & 0 & 0 & \xi & \eta & \xi\eta & 0 & 0 & 0 & 0 & 0 \\ 0 & 0 & 0 & 0 & 0 & 0 & 0 & 0 & 0 & 0 & 0 & 0 & 0 & 0 & \xi & 0 & \xi\eta & 0 \\ 0 & 0 & 0 & 0 & 0 & 0 & 0 & 0 & 0 & 0 & 0 & 0 & 0 & 0 & 0 & \eta & 0 & \xi\eta \end{bmatrix}. \tag{B.3}$$

References

1. Achuthan, A., Keng, A., Ming, W.: Shape control of coupled nonlinear piezoelectric beams. Smart Mater. Struct. **10**(5), 914–924 (2001)
2. Bilgen, O., Kochersberger, K.B., Inman, D.J.: Macro-fiber composite actuators for a swept wing unmanned aircraft. Aeronaut. J. **113**(1144), 385–395 (2009)
3. Chrscielewski, J., Schmidt, R., Eremeyev, V.A.: Nonlinear finite element modeling of vibration control of plane rod-type structural members with integrated piezoelectric patches. Contin. Mech. Thermodyn. (2018). https://doi.org/10.1007/s00161-018-0672-4
4. Crawley, E.F., Lazarus, K.B.: Induced strain actuation of isotropic and anisotropic plates. AIAA J. **29**, 944–51 (1991)
5. De Gespari, A., Ricci, S., Riccobene, L., Scotti, A.: Active aeroelastic control over a multi-surface wing: modeling and wind-tunnel testing. AIAA J. **47**(9), 1995–2010 (2009)
6. Dvorkin, E.N., Oñate, E., Oliver, X.: On a nonlinear formulation for curved Timoshenko beam elements considering large displacement/rotation increments. Int. J. Numer. Methods **26**, 1597–1613 (1988)
7. Ge, P., Jouaneh, M.: Modeling hysteresis in piezoceramic actuators. Precis. Eng. **17**, 211–21 (1995)
8. Gilardi, G., Buckham, B.J., Park, E.J.: Finite element modeling of a slewing non-linear flexible beam for active vibration control with arrays of sensors and actuators. J. Intell. Mater. Syst. Struct. **20**(16), 1941–58 (2009)
9. Gopinathan, S.V., Varadan, V.V., Varadan, V.K.: A review and critique of theories for piezoelectric laminates. Smart Mater. Struct. **9**(1), 24 (2000)
10. Gupta, V.K., Seshu, P., Issac, K.K.: Finite element and experimental investigation of piezoelectric actuated smart shells. AIAA J. **42**(10), 2112–2123 (2004)
11. Habip, L.M.: Theory of elastic shells in the reference state. Ing. Arch. **34**, 228–237 (1965)
12. Hong, C.H., Chopra, I.: Modeling and validation of induced strain actuation of composite coupled plates. AIAA J. **37**, 372–7 (2001)
13. Hu, Q., Ma, G.: Variable structure control and active vibration suppression of flexible spacecraft during altitude maneuver. Aerosp. Sci. Technol. **9**(4), 307–17 (2005)
14. Hughes, T.J.R., Tezduyar, T.: Finite elements based upon Mindlin plate theory with particular reference to the four-node bilinear isoprametric element. J. Appl. Mech. **48**, 587–596 (1981)
15. Joshi, P.: Nonlinear constitutive relations for piezoceramic materials. Smart Mater. Struct. **1**, 80–3 (1992)
16. Kapuria, S., Kumari, P., Nath, J.K.: Efficient modeling of smart piezoelectric composite laminates: a review. Acta Mech. **214**, 31–48 (2010)
17. Kapuria, S., Yaqoob Yasin, M.: A nonlinear efficient layerwise finite element model for smart piezolaminated composites under strong applied electric field. Smart Mater. Struct. **22**, 055,021 (2013)
18. Kapuria, S., Yaqoob Yasin, M., Hagedorn, P.: Active vibration control of piezolaminated composite plates considering strong electric field nonlinearity. AIAA J. (2014). https://doi.org/10.2514/1.J053166
19. Klinkel, S., Wagner, W.: A geometrically non-linear piezoelectric solid shell element based on a mixed multi-field variational formulation. Int. J. Numer. Methods Eng. **65**, 349–82 (2006)
20. Klinkel, S., Wagner, W.: A piezoelectric solid shell element based on a mixed variational formulation for geometrically linear and nonlinear applications. Comput. Struct. **86**, 38–46 (2008)
21. Kogl, M., Bucalem, M.L.: Analysis of smart laminates using piezoelectric MITC plate and shell elements. Comput. Struct. **83**, 1153–63 (2005)
22. Lee, S., Yang, S.H., Kim, Y.S., Park, H.C., Yoon, K.J.: Material nonlinear characteristics of the 3203HD PZT wafer under high electric field. Sens. Actuators A **121**, 450–56 (2005)
23. Lentzen, S.: Nonlinear coupled thermopiezoelectric modeling and FE-simulation of smart structures. Ph.D. thesis, RWTH Aachen University (2008)
24. Li, S., Cao, W., Cross, L.E.: The extrinsic nature of nonlinear behavior observed in lead zirconate titanate ferroelectric ceramic. J. Appl. Phys. **69**, 7219–24 (1991)
25. Macvean, R.H.: A simple quadrilateral shell element. Comput. Struct. **8**, 175–183 (1978)
26. Masys, A.J., Ren, W., Yang, G., Mukherjee, B.K.: Piezoelectric strain in lead zirconate titanate ceramics as a function of electric field, frequency, and DC bias. J. Appl. Phys. **94**, 1152–62 (2003)
27. Parashar, S.K., DasGupta, A., von Wagner, U., Hagedorn, P.: Nonlinear shear vibrations of piezoceramic actuators. Int. J. Nonlinear Mech. **40**, 429–43 (2005)
28. Parashar, S.K., von Wagner, U., Hagedorn, P.: Finite element modeling of nonlinear vibration behavior of piezo-integrated structures. Comput. Struct. **119**, 37–47 (2013)
29. Pendleton, E.W., Besette, D., Field, P.B., Miller, G.D., Griffin, K.E.: Active aeroelastic wing flight research program: technical program and model analytical development. J. Aircr. **37**(4), 554–561 (2000)
30. Pradyumna, S., Gupta, A.: Nonlinear dynamic stability of laminated composite shells integrated with piezoelectric layers in thermal environment. Acta Mech. **218**(3–4), 295–308 (2010). https://doi.org/10.1007/s00707-010-0424-4
31. Rao, M.N., Schmidt, R.: Static and dynamic finite rotation FE-analysis of thin-walled structures with piezoelectric sensor and actuator patches or layers. Smart Mater. Struct. **23**, 095,006 (2014)
32. Rao, M.N., Schmidt, R., Schröder, K.U.: Finite rotation FE-simulation and active vibration control of smart composite laminated structures. Comput. Mech. **55**, 719–735 (2015)
33. Roysten, T.J., Houston, B.H.: Modeling and measurement of nonlinear dynamic behavior in piezoelectric ceramics with application to 1–3 composites. J. Acoust. Soc. Am. **104**, 2814–27 (1998)
34. Samal, M.K., Seshu, P., von Wagner, U., Hagedorn, P., Dutta, B.K., Kushwaha, H.S.: A mathematical model in three dimensional piezoelectric continuum to predict non-linear responses of pieceramic materials. Proc. Inst. Mech. Eng. C **222**, 2251–68 (2008)
35. Sateesh, V.L., Upadhyay, C.S., Venkatesan, C.: A study of the polarization-electric-field nonlinear effect on the response of smart composite plates. Smart Mater. Struct. **19**(7), 075,012 (2010)

36. Shivakumar, J., Ashok, M.H., Ray, M.C.: Active control of geometrically nonlinear transient vibrations of laminated composite cylindrical panels using piezoelectric fiber reinforced composite. Acta Mech. **224**(1), 1–15 (2012). https://doi.org/10.1007/s00707-012-0724-y
37. Simo, J.C., Rifai, M.S.: A class of mixed assumed strain methods and the methods of incompatible modes. Int. J. Numer. Methods Eng. **29**, 1595–1638 (1990)
38. Sun, D., Tong, L., Wang, D.: An incremental algorithm for static shape control of smart structures with nonlinear piezoelectric actuators. Int. J. Solids Struct. **41**, 2277–92 (2004)
39. Thakkar, D., Ganguly, R.: Induced shear actuation of helicopter rotor blade for active twist control. Thin-Walled Struct. **45**(1), 111–121 (2007)
40. Thornburgh, R.P., Chattopadhyay, A.: Nonlinear actuation of smart composites using a coupled piezoelectric mechanical model. Smart Mater. Struct. **10**, 743–9 (2001)
41. Tiersten, H.F.: Electroelastic equations for electroded thin plates subject to large deriving voltages. J. Appl. Phys. **74**, 3389–93 (1993)
42. Tzou, H.S., Ye, R.: Analysis of piezoelastic structures with laminated piezoelectric triangle shell elements. AIAA J. **34**, 110–115 (1996)
43. von Wagner, U., Hagedorn, P.: Piezo-beam systems subjected to weak electric field: experiments and modeling of nonlinearities. J. Sound Vib. **256**, 861–72 (2002)
44. Wagner, W., Gruttmann, F.: A robust non-linear mixed hybrid quadrilateral shell element. Int. J. Numer. Methods Eng. **64**, 635–666 (2005)
45. Wang, Q.M., Zhang, Q., Xu, B., Liu, R., Cross, L.E.: Nonlinear piezoelectric behavior of ceramic bending mode actuators under strong electric fields. J. Appl. Phys. **86**, 3352–60 (1999)
46. Yang, J.S., Batra, R.C.: Mixed variational principles in non-linear electroelasticity. Int. J. Nonlinear Mech. **30**, 719–25 (1995)
47. Yang, J.S., Batra, R.C.: A second order theory for piezoelectric materials. J. Acoust. Soc. Am. **97**, 280–8 (1995)
48. Yao, L.Q., Zhang, J.G., Lu, L., Lai, M.O.: Nonlinear dynamic characteristics of piezoelectric bending actuators under strong applied electric field. J. Microelectromech. Syst. **13**, 645–52 (2004)
49. Yao, L.Q., Zhang, J.G., Lu, L., Lai, M.O.: Nonlinear extension and bending of piezoelectric laminated plate under large applied field actuation. Smart Mater. Struct. **13**, 404–14 (2004)
50. Yao, L.Q., Zhang, J.G., Lu, L., Lai, M.O.: Nonlinear static characteristics of piezoelectric bending actuators under strong applied electric field. Sens. Actuators A **115**, 168–75 (2004)